THE UNIVERSITY OF WARWICK

Library Declaration and Deposit Agreement

1. **STUDENT DETAILS**

   Caitlyn Jane Cullen
   u1839845

2. **THESIS DEPOSIT**

   2.1 I understand that under my registration at the University, I am required to deposit my thesis with the University in BOTH hard copy and in digital format. The digital version should normally be saved as a single pdf file.

   2.2 The hard copy will be housed in the University Library. The digital version will be deposited in the University's Institutional Repository (WRAP). Unless otherwise indicated (see 2.3 below) this will be made openly accessible on the Internet and will be supplied to the British Library to be made available online via its Electronic Theses Online Service (EThOS) service. [At present, theses submitted for a Master's degree by Research (MA, MSc, LLM, MS or MMedSci) are not being deposited in WRAP and not being made available via EthOS. This may change in future.]

   2.3 In exceptional circumstances, the Chair of the Board of Graduate Studies may grant permission for an embargo to be placed on public access to the hard copy thesis for a limited period. It is also possible to apply separately for an embargo on the digital version. (Further information is available in the Guide to Examinations for Higher Degrees by Research.)

   2.4 (a) Hard Copy I hereby deposit a hard copy of my thesis in the University Library to be made publicly available to readers immediately.
   I agree that my thesis may be photocopied.

   (b) Digital Copy I hereby deposit a digital copy of my thesis to be held in WRAP and made available via EThOS.
   My thesis can be made publicly available online.

3. **GRANTING OF NON-EXCLUSIVE RIGHTS**

   Whether I deposit my Work personally or through an assistant or other agent, I agree to the following: Rights granted to the University of Warwick and the British Library and the user of the thesis through this agreement are non-exclusive. I retain all rights in the thesis in its present version or future versions. I agree that the institutional repository administrators and the British Library or their agents may, without changing content, digitise and migrate the thesis to any medium or format for the purpose of future preservation and accessibility.

4. **DECLARATIONS**

(a) I DECLARE THAT:

- I am the author and owner of the copyright in the thesis and/or I have the authority of the authors and owners of the copyright in the thesis to make this agreement. Reproduction of any part of this thesis for teaching or in academic or other forms of publication is subject to the normal limitations on the use of copyrighted materials and to the proper and full acknowledgement of its source.
- The digital version of the thesis I am supplying is the same version as the final, hardbound copy submitted in completion of my degree, once any minor corrections have been completed.
- I have exercised reasonable care to ensure that the thesis is original, and does not to the best of my knowledge break any UK law or other Intellectual Property Right, or contain any confidential material.
- I understand that, through the medium of the Internet, files will be available to automated agents, and may be searched and copied by, for example, text mining and plagiarism detection software.

(b) IF I HAVE AGREED (in Section 2 above) TO MAKE MY THESIS PUBLICLY AVAILABLE DIGITALLY, I ALSO DECLARE THAT:

- I grant the University of Warwick and the British Library a licence to make available on the Internet the thesis in digitised format through the Institutional Repository and through the British Library via the EThOS service.
- If my thesis does include any substantial subsidiary material owned by third-party copyright holders, I have sought and obtained permission to include it in any version of my thesis available in digital format and that this permission encompasses the rights that I have granted to the University of Warwick and to the British Library.

5. **LEGAL INFRINGEMENTS**

I understand that neither the University of Warwick nor the British Library have any obligation to take legal action on behalf of myself, or other rights holders, in the event of infringement of intellectual property rights, breach of contract or of any other right, in the thesis.

Please sign this agreement and return it to the Graduate School Office when you submit your thesis.

Student's signature: C.Cullen .....Date: 19/02/2023

A Search for Non-Transiting Planets with Optical Phase Curves from the TESS Mission

by

Caitlyn Jane Cullen

Thesis

Submitted to the University of Warwick

for the degree of

Master of Science (by Research) in Physics

Department of Physics

October 2022

THE UNIVERSITY OF WARWICK

Contents

List of Tables

List of Figures

Acknowledgments

I'd like to start by thanking my supervisor, Dr Daniel Bayliss. I am so grateful you agreed to take me on as a Master's student. This past year I've learnt many things from you but one of the most important is how to enjoy what I do. Thank you for your guidance, support and continued enthusiasm.

I would like to extend thanks to the entire astronomy group at Warwick for making my journey so enjoyable. The group atmosphere is truly something special, a fact that has become only more obvious as I come to the end of my project. Thank you for all the jokes, the advice and encouragement, and all the cake - there's nothing quite like starting the week with Monday Morning Baking instead of breakfast!

To Faith, thank you for your friendship, your support and all your patient guidance. Thank you for wheeling across the room every time I had an interesting light-curve to look at and suggesting progressively more outrageous scenarios for it. Thank you for reading my articles, showing me memes, and sending me bits of Python code. But most of all, thank you for your unwavering ability to make me laugh and set me back on track whenever things didn't go to plan. My Master's experience would not have been the same without you. Take care of Comments Geralt for me!

And finally, to Jack: you've been my biggest supporter over the last year and I'm hugely grateful to you for it. Thank you for believing in me, for trusting me, and for supporting me when I took on too much work. Thank you for laughing with me when I've done something silly, and for listening to me rant when I'm stuck. Thank you for helping me find the courage to go after what I want and the confidence to try new things. I look forward to our next adventure.

Declarations

I declare that the work in this thesis is my own and was carried out at the University of Warwick, during the period October 2021 to September 2022, under the supervision of Dr Daniel Bayliss. The research reported here has not been submitted, either wholly or in part, to any other academic institution for any other degree or qualification.

The work in this thesis will be submitted for publication in the Monthly Notices of the Royal Astronomical Society (MNRAS) in October 2022. Namely, Chapter 2, detailing the methodology and results of this work, will be submitted for publication with minor changes.

Data Acknowledgements

We acknowledge the use of public *TESS* Alert data from pipelines at the *TESS* Science Office and at the *TESS* Science Processing Operations Centre. This paper includes data collected with the *TESS* mission, obtained from the MAST data archive at the Space Telescope Science Institute (STScI). Funding for the *TESS* mission is provided by the NASA Explorer Program. STScI is operated by the Association of Universities for Research in Astronomy, Inc., under NASA contract NAS 5–26555.

This research makes use of the Exoplanet Follow-up Observation Program website, which is operated by the California Institute of Technology, under contract with the National Aeronautics and Space Administration under the Exoplanet Exploration Program.

This paper includes data collected by the *TESS* mission that are publicly available from the Mikulski Archive for Space Telescopes (MAST).

This work makes use of data from the European Space Agency's (ESA) *Gaia* mission, processed by the *Gaia* Data Processing and Analysis Consortium DPAC. Funding for the DPAC has been provided by national institutions, in particular the institutions participating in the *Gaia* Multilateral Agreement.

Abstract

Phased photometric variation provides a method for discovering non-transiting exoplanets in high-precision timeseries photometry. Applying a Lomb-Scargle algorithm, we search for phased photometric variations in a selection of 140,000 full frame image light-curves in data from the southern ecliptic hemisphere of the Transiting Exoplanet Survey Satellite (*TESS*) mission. We fit the phased photometric variation signal for these candidates using a three-component model comprised of atmospheric modulation, tidal ellipsoidal distortion, and Doppler beaming contributions. We find 27 candidate systems that may host short-period, massive planets. Our candidates have periods ranging from 0.74 to 1.98 days, and photometric variations with amplitudes ranging from 94 to 528 ppm. The host stars are all bright ($9<T<11$) F and G type dwarf stars. We estimate the radial velocity semi-amplitudes to be in excess of $60\,\mathrm{m\,s^{-1}}$ for each candidate, easily within reach of current high-precision spectrographs. If confirmed, these candidates would be the first non-transiting exoplanets detected with *TESS*.

Abbreviations

CCD Charge Coupled Device

ESO European Southern Observatory

FoV Field-of-view

FFI Full Frame Image

LS Lomb-Scargle

MAST Mikulski Archive for Space Telescopes

PDCSAP Pre-search Data Conditioning

PLATO *PLAnetary Transits and Oscillations of stars*

SAP Standard Aperture Photometry

SPOC Science Processing Operations Centre

TESS *Transiting Exoplanet Survey Satellite*

TIC *TESS* Input Catalogue

AU Astronomical unit, 1.496×10^8 km

$M_\oplus$ Earth mass, 5.972×10^{24} kg

$R_\oplus$ Earth radius, 6 378 km

M_J Jupiter mass, 1.898×10^{27} kg

R_J Jupiter radius, 71 492 km

$M_\odot$ Solar mass, 1.989×10^{30} kg

$R_\odot$ Solar radius, 695 700 km

Chapter 1

Introduction

1.1 Exoplanets

Humans have always been fascinated by the sky, and throughout history we have explored space in many different ways. We have landed on the Moon, sent probes to nearby planets, and even launched a spacecraft outside of our solar system.

One topic that has remained of particular interest to astronomers over time is the prospect of other planets. From as early as 2000 BC, Babylonian astronomers made naked eye observations of the five innermost planets in our solar system beside the Earth: Mercury, Venus, Mars, Jupiter, and Saturn (Sachs, 1974; Gingerich, 1985). By the end of the 19th Century, the invention of telescopes enabled the discovery of the two remaining planets, Uranus and Neptune, along with a host of moons, asteroids and dwarf planets scattered throughout the solar system (Herschel and Watson, 1781; Airy, 1847).

This journey continues into the 21st Century as we search for worlds outside of our solar system: exoplanets. The concept of exoplanets was first suggested in the 16th Century by Italian philosopher Giordano Bruno who believed that the stars in the sky may be similar to our Sun, each hosting a collection of their own planets (Bruno, 1584).

The first exoplanet detection occurred in 1992 when Wolszczan and Frail (1992) confirmed the discovery of two planets orbiting an extremely dense, rapidly rotating neutron star called a pulsar. Two years later, the existence of a third planet in the system was also confirmed (Wolszczan, 1994). These planets, however, are rare, exotic objects, doused in radiation and thought to have formed after explosive events called supernova (Wolszczan, 2008; Patruno and Kama, 2017).

The first exoplanet to be discovered around a main sequence star (a star more

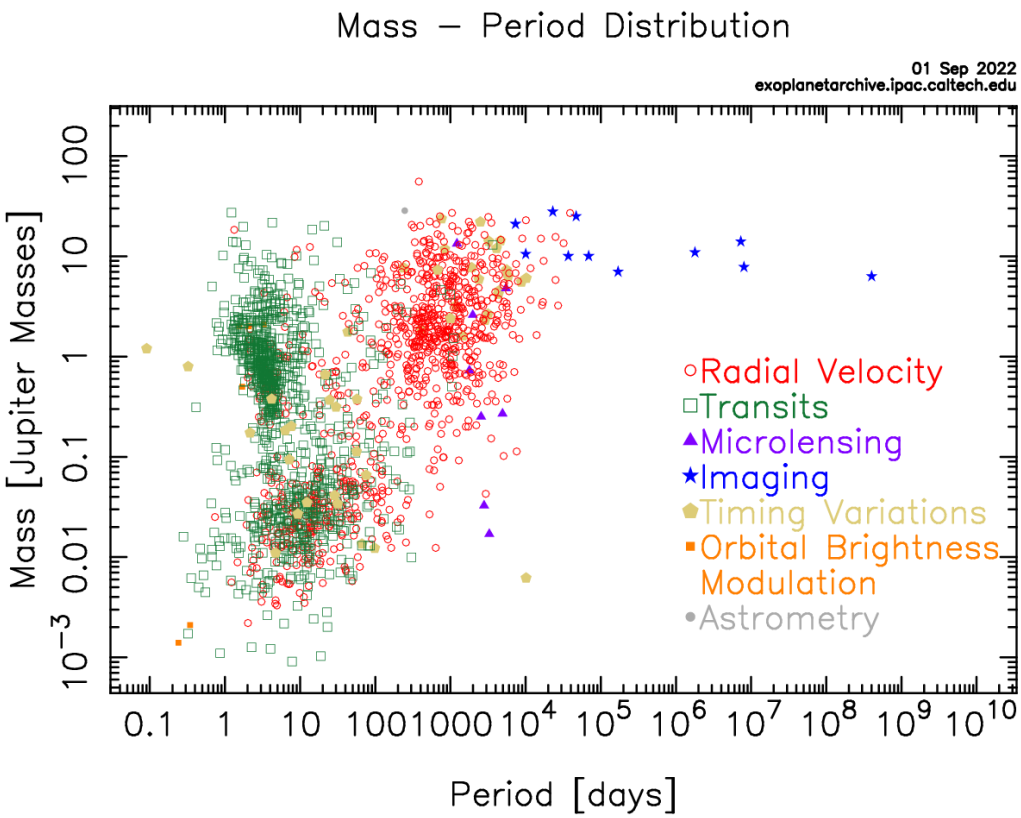

Figure 1.1: Distribution of orbital periods and masses for all known exoplanets with with mass or $M_p sin(i)$ measurements, separated by detection method. Image credit: NASA Exoplanet Archive

similar to our sun) was 51 Pegasi b (Mayor and Queloz, 1995). The Jupiter-sized planet is known to be a gas giant and orbits its star at a distance of 0.052 AU (Naef et al., 2004; Rosenthal et al., 2021) - 10 times closer than Mercury orbits the Sun. 51 Pegasi b has a mass just under half that of Jupiter, however due to the star's intense irradiation, the planet has an inflated radius of 1.2 R_J. 51 Pegasi b became the first known "hot Jupiter" planet.

1.1.1 Hot Jupiters

As their name suggests, hot Jupiters are large, Jupiter-size planets closely orbiting their parent stars. Due to their short orbital periods ($\leq$ 15 days), these planets often have high equilibrium temperatures and inflated radii (Bodenheimer et al., 2001; Sestovic et al., 2018).

Jupiter-size planets were once widely believed to exist solely in the outer regions of planetary systems much like Jupiter and Saturn in our own Solar System.

Thus, it came as somewhat a surprise when the first exoplanet detection around a main-sequence star, 51 Pegasi b, was a giant, short-period planet. For a long time hot Jupiters were the most frequently detected exoplanets, however, it later became known that despite their apparent abundance, hot Jupiters are in fact rare planets (Hsu et al., 2019; Beleznay and Kunimoto, 2022). In particular, large masses and radii paired with short orbital periods lend hot Jupiters a strong bias to detection.

Figure 1.1 shows the distribution of planetary masses and orbital periods for all known exoplanets (as of 01 September 2022). There is a significant, dense region of detections at short periods and high masses corresponding to the detection of hot Jupiters. Furthermore, it is evident that there are two main modes of exoplanet detection: radial velocity measurements and transit photometry.

1.1.2 Radial Velocity Measurements

In every star-planet system, both bodies orbit the centre of mass of the system. For large, close-in planets, this centre of mass can be significantly offset from the centre of the individual star. The motion of the planet throughout its orbit causes the star to "wobble". This effect appears as a shift in the wavelength of the star's light due to changes in its velocity according to the observer (Marcy and Butler, 1996) - a phenomenon known as the Doppler effect.

Variations in a star's radial velocity are observed by calculating the offset at which a collection of absorption lines in the stellar spectra appear. By monitoring the radial velocity of a star over several orbits, the existence of a planetary candidate can be confirmed.

Figure 1.2 illustrates the radial velocity measurements of 51 Pegasi over a one-year period from September 1994 to September 1995 by Mayor and Queloz (1995). The measurements show a clear sinusoidal variation in the star's radial velocity and were used to confirm the planet's existence.

For planets with circular orbits, the semi-amplitude of radial velocity variations, K, can be calculated according to the following equation (Lovis and Fischer, 2010):

$$K = \left(\frac{2\pi G}{P}\right)^{\frac{1}{3}} \frac{M_P \sin(i)}{(M_* + M_P)^{\frac{2}{3}}}, \tag{1.1}$$

where G is the gravitational constant, P is the orbital period of the planet, M_P is the planetary mass, i is the orbital inclination, and M_* is the stellar mass.

As is evident from Equation 1.1, the radial velocity method is particularly sensitive to high mass planets with short orbital periods such as hot Jupiters. For

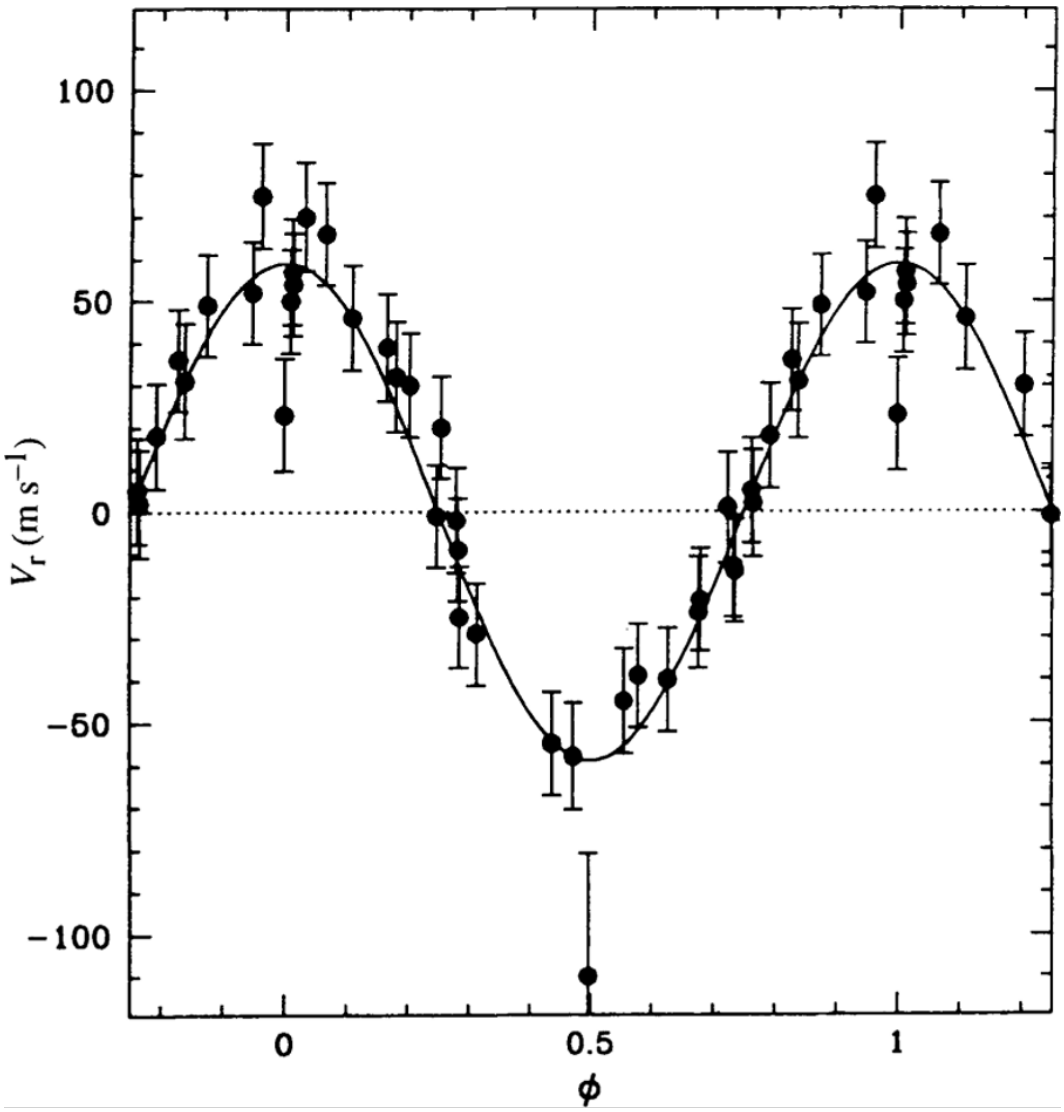

Figure 1.2: Radial velocity semi-amplitude measurements as a function of orbital phase (ϕ) taken of the first known hot Jupiter system, 51 Pegasi. The measurements were taken during four short windows over a period of one year from September 1994 to September 1995 by Mayor and Queloz (1995). The solid black line indicates the best fit model for a circular orbit.

example, 51 Pegasi (shown in Figure 1.2) shows a radial velocity semi-amplitude of $K = 50\,\mathrm{ms}^{-1}$. Furthermore, the systems most amenable to radial velocity follow up are those with low stellar effective temperatures ($\mathrm{T_{eff}} \leq 6500\,\mathrm{K}$) such that the crucial spectral features are most evident (Beatty and Gaudi, 2015).

Equation 1.1 also presents the relationship between the angle of orbital inclination and the radial velocity semi-amplitude. Although the effect is strongest for planets orbiting their stars at ~ 90 degrees, there is just a small decease ($\sim 15\%$) in amplitude for planets orbiting at ~ 60 degrees. Therefore the radial velocity method is suitable to confirm the presence of non-transiting hot Jupiter candidates.

The radial velocity method alone is rather inefficient at detecting hot Jupiters as it is time consuming, and targets a single star at any incidence. This deficiency quickly led to the advent of a new method that could be applied to wide-field surveys: transit photometry.

1.1.3 Transit Photometry

By far the most lucrative detection mode, the transit method utilises periodic dips in a system's light to find exoplanets. When a planet passes directly between its star and an observer it is called a transit event.

During a transit, the planet blocks a portion of the star's light from the observer and the system appears to dim (see Figure 1.3). Often, this decrease in flux is detectable from Earth. The change in flux, ΔF, during a transit event can be calculated with the following equation (Winn, 2010):

$$\frac{\Delta F}{F_0} = \left(\frac{\mathrm{R}_p}{\mathrm{R}_\odot}\right)^2 \tag{1.2}$$

where F_0 is the out-of-transit flux level.

For systems where $\mathrm{R}_p \ll \mathrm{R}_*$, and all orbits are circular, the probability of a transit event is (Winn, 2010; Sackett, 1999):

$$p_{trans} \approx 0.005 \left(\frac{\mathrm{R}_*}{\mathrm{R}_\odot}\right) \left(\frac{a}{1\,AU}\right)^{-1} \tag{1.3}$$

where a is the semi-major axis.

Over time, there have been many programs dedicated to finding planets with the transit method including ground-based facilities such as the Wide Angle Search for Planets project (*WASP*; Pollacco et al., 2006) and the Next Generation Transit Survey (*NGTS*; Wheatley et al., 2018), as well as space-based surveys such as *Kepler* (Borucki et al., 2010), *K2* (Howell et al., 2014), and the Transiting Exoplanet Survey

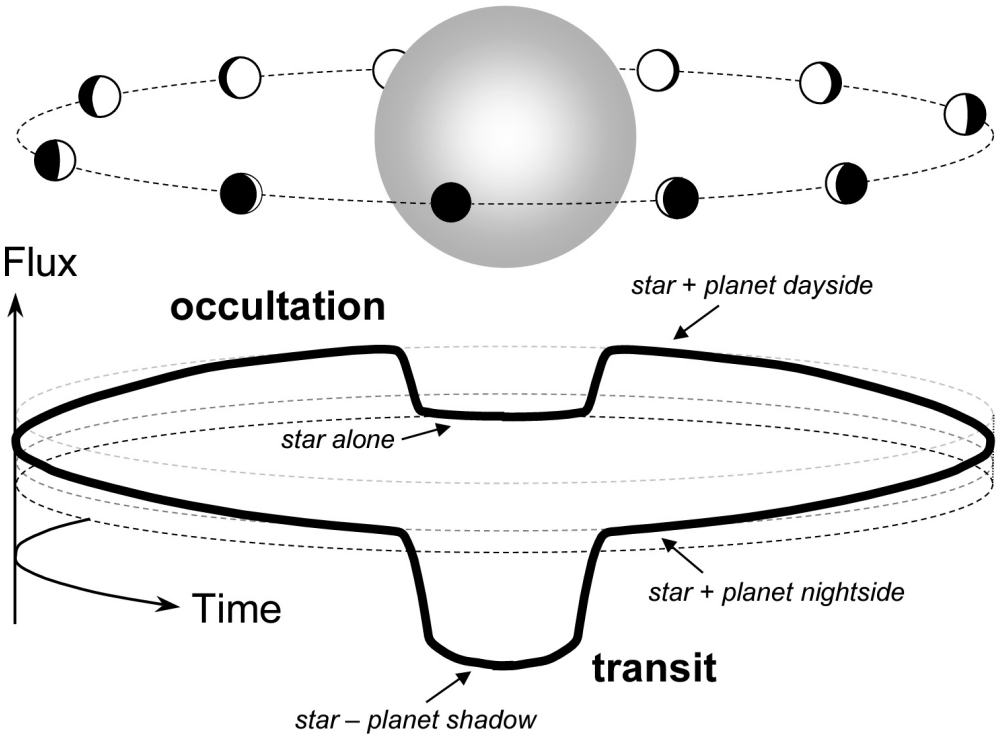

Figure 1.3: Illustration of transits and occultations (or eclipses). During a transit event, the flux drops due to the planet blocking a portion of the star's light. The flux then rises as the planet passes out of transit and its dayside comes in to view, before dropping slightly again during the occultation as the reflected light from the planet is blocked by the star (Winn, 2010).

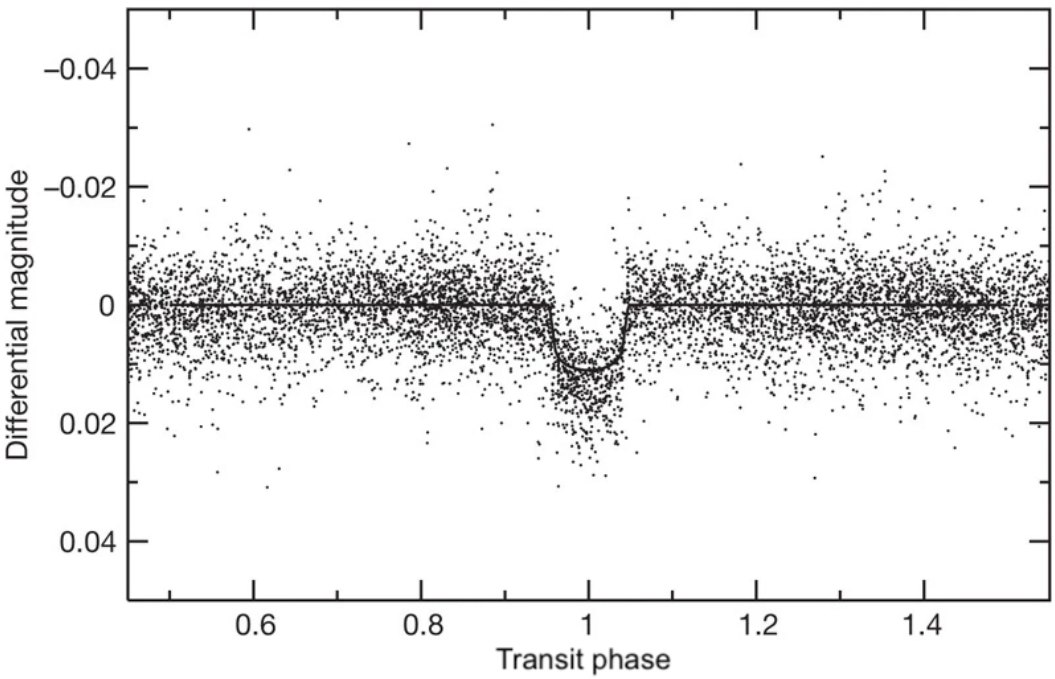

Figure 1.4: WASP-South light-curve for the known transiting planet WASP-18 b. The light-curve is phase folded on a period of 0.94 days, displaying a prominent dip ($\sim 1\%$) in magnitude at phase=1.0 (Hellier et al., 2009a). The solid black line represents the best fit transit model.

Satellite mission (*TESS*; Ricker et al., 2015).

The first planet with observed transits was HD 209458 b - a hot Jupiter originally discovered with radial velocity observations (Henry et al., 2000). Using estimated transit times from the RV measurements, both Henry et al. (2000) and (Charbonneau et al., 2000) were able to observe small decreases in the apparent brightness of the host star. A few years later, the first planet to be discovered with the transit method was observed by the *OGLE* facility (Udalski et al., 1992).

Figure 1.4 shows a transit detection for WASP-18 b by Hellier et al. (2009a), phase folded at a period of 0.94 days. WASP-18 b is a massive, short-period system with a transit depth of approximately 1%.

Figure 1.5 shows the cumulative distribution of exoplanet discoveries per year, separated by mode of detection. To date, nearly 4000 planets have been discovered with transit photometry - far more than any other detection method.

The transit method has provided the opportunity to observe a wide range of planets, from ultra short period hot Jupiters such as WASP-18 b (Hellier et al., 2009a) and TOI-2109b (Wong et al., 2021a) both orbiting their stars with periods

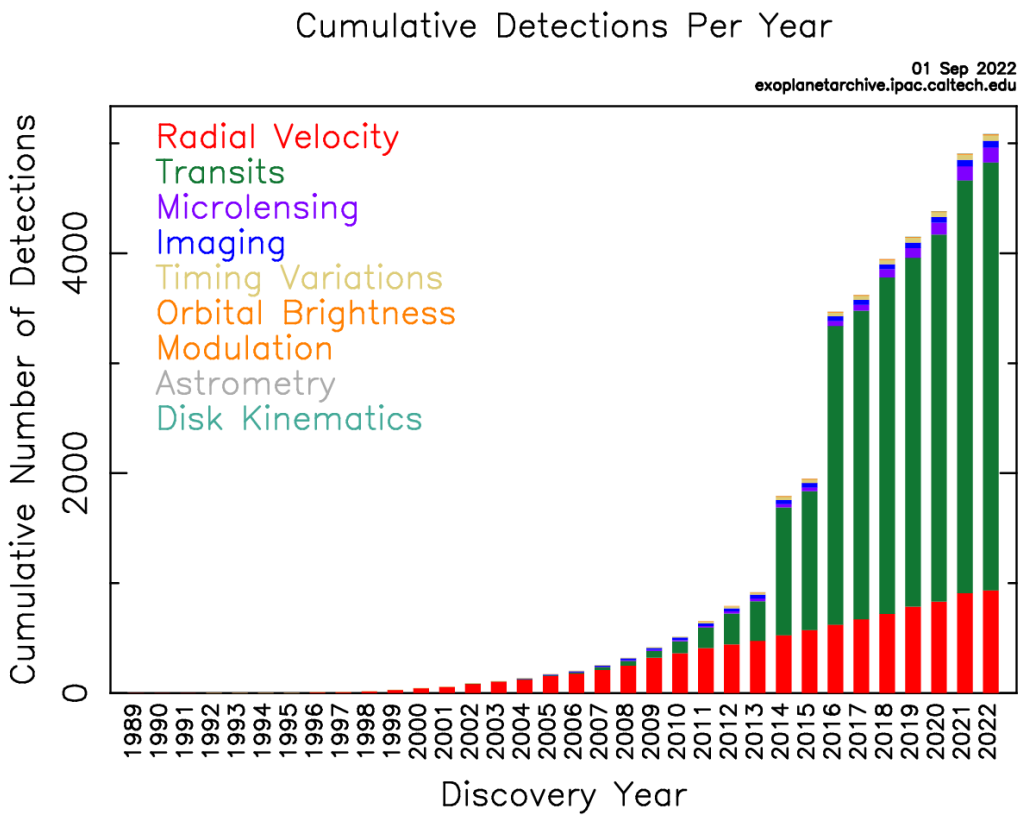

Figure 1.5: Cumulative detections of exoplanets shown by year and detection method. To date, the total number of confirmed exoplanets is 5,090. Image credit: NASA Exoplanet Archive.

less than one day, to planets much further away from their stars, such as Kepler-167e which takes approximately 3 years to complete one orbit of its parent star (Kipping et al., 2016).

1.2 Optical Phase Curves of Non-Transiting Planets

Due to their large size and short periods, hot Jupiter planets are particularly amenable to indirect detection methods such as transit photometry and radial velocity measurements. However, with photometric transit surveys, only a small portion of the true exoplanet population is observed. As shown in Equation 1.3, the geometric probability of transits for a hot Jupiter with a radius of 1.3 R_J on a 2-day orbit around a solar-type star is 9.4%. As such, photometric transit searches will miss over 90% of such planets. These normally-overlooked planets are known as "non-transiting" planets and are significantly more difficult to discover than their transiting counterparts.

Non-transiting planets do not exhibit transit events and therefore do not cause observable dips in the light of their systems. However, hot Jupiters cause other variations in photometry throughout their orbits. These phased photometric variations are often referred to as *phase curves*. Phase curve signals can be detectable for both transiting planets (e.g: WASP-18 b (Shporer et al., 2019; Wong et al., 2020), WASP-12 b (Hebb et al., 2009; Wong et al., 2021b) and TOI-2109 b (Wong et al., 2021a)) and non-transiting planets (e.g: KIC 8121913 b, KIC 10068024 b, and KIC 5479689 b (Lillo-Box et al., 2021)).

There are three main phase curve components: atmospheric modulation, tidal ellipsoidal distortion, and Doppler beaming.

1.2.1 Atmospheric Modulation

The atmospheric modulation effect is comprised of two processes: reflection of starlight from the planet's atmosphere, and thermal emission due to dayside heating of the planet. For large, close-in planets, all orbits are assumed to be circularised (Mazeh, 2008) and the planets are assumed to be tidally locked to their stars such that there exists a fixed dayside hemisphere (Shporer, 2017). Figure 1.6 demonstrates the various phases of atmospheric modulation on the planet's face presented to the observer and the corresponding phase curve component. Combined, these two processes create a variation in the system's light that is sinusoidal in shape and reaches a maximum when the planet is behind the star such that the daylight hemisphere is presented to the observer.

Shporer (2017) gives an empirical approximation for the amplitude of atmospheric modulation as:

$$A_{atm} \approx 57\alpha_{atm} \sin i \times \left(\frac{\mathrm{M}_*}{M_\odot}\right)^{-2/3} \left(\frac{P}{day}\right)^{-4/3} \left(\frac{\mathrm{R}_p}{R_J}\right)^2 ppm, \tag{1.4}$$

where R_p is the radius of the planet. α_{atm} is an order of unity coefficient that depends on the efficiency of atmospheric heat redistribution and reflectivity.

As the only phase curve component dependent on the planet radius, and with a strong relationship to period, atmospheric modulation is particularly sensitive to large, short period planets. As such, for most hot Jupiter planets, the atmospheric modulation effect is often large and dominates the phase curve signal.

1.2.2 Tidal Ellipsoidal Distortion

The tidal ellipsoidal distortion effect results from the gravitational interaction of two massive bodies such a planet and its host star. During its orbit, a planet exerts

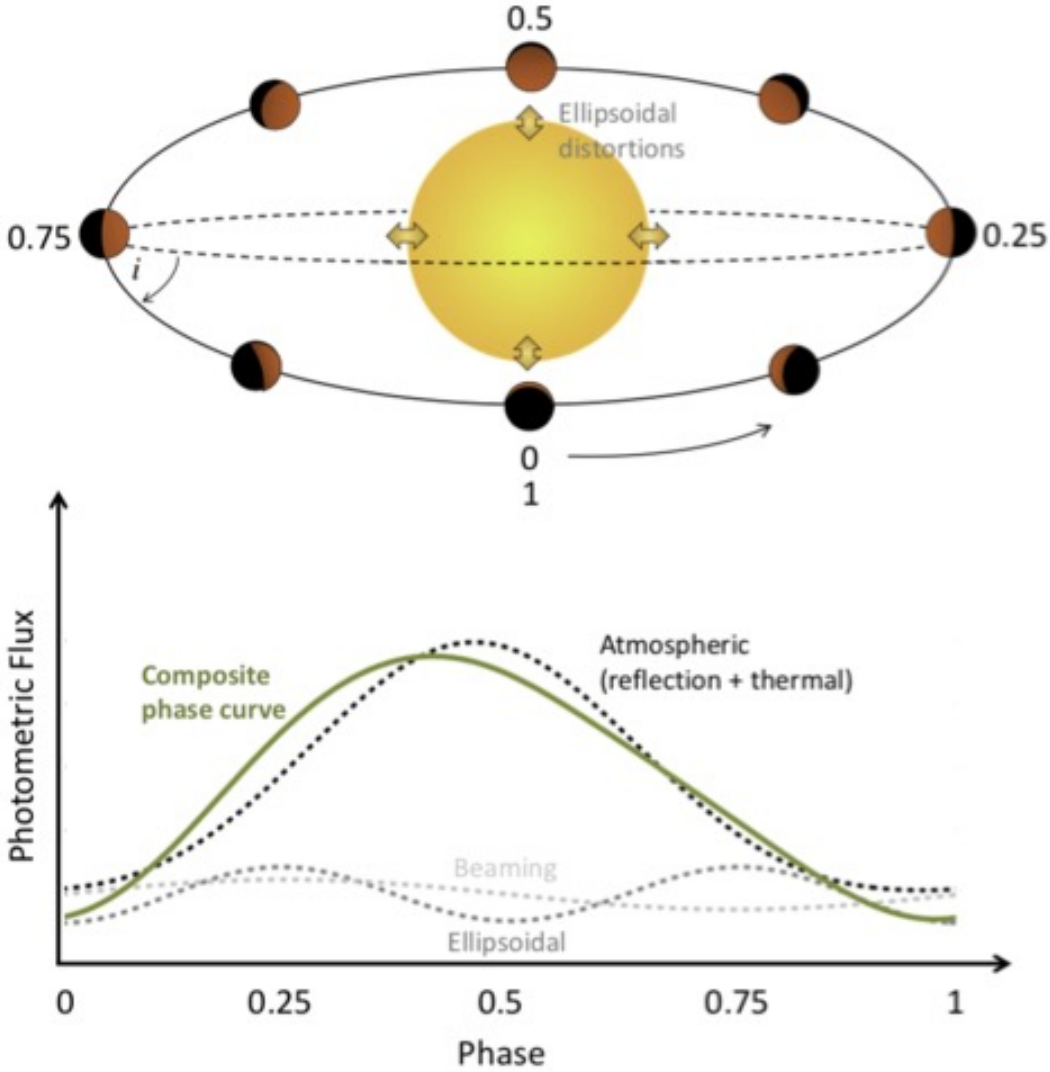

Figure 1.6: Schematic of three phase curve components: atmospheric modulation, tidal ellipsoidal distortion, and Doppler beaming. Top panel: Orbital path of a non-transiting planet with associated atmospheric phases and tidal ellipsoidal distortions. Bottom panel: individual phase curve components (dashed lines) and total phase curve shape (solid green line) (Lillo-Box et al., 2021).

a gravitational force on its host star, distorting it into an ellipsoidal shape along the star-planet axis. As a result, twice per orbit, an elongated side of the star is presented to the observer. This distortion in shape creates a modulation in the amount of light the observer sees depending on the area of the star that is visible. The modulation in flux is approximated by the following equation (Shporer, 2017):

$$A_{ellip} = 13\alpha_{ellip} \sin i \times \left(\frac{\mathrm{R}_*}{R_\odot}\right)^3 \left(\frac{\mathrm{M}_*}{M_\odot}\right)^{-2} \left(\frac{P}{day}\right)^{-2} \left(\frac{M_p \sin i}{M_J}\right) ppm, \tag{1.5}$$

where M_p is the mass of the planet. α_{ellip} is a coefficient that accounts for differences in brightness across the visible disc of the star due to stellar limb darkening, u, and gravity darkening, g, and can be calculated with the following equation:

$$\alpha_{ellip} = 0.15\frac{(15+u)(1+g)}{3-u}. \tag{1.6}$$

Despite generally being a subtle effect, tidal ellipsoidal distortion is dependent of the planetary mass and as such contributes significantly for high mass companions such as WASP-18 b (Hellier et al., 2009a; Shporer et al., 2019; Wong et al., 2020) and KELT-1 b (Siverd et al., 2012; Wong et al., 2021b). The effect is most prominent for systems with a high ratio of planetary to stellar masses.

Furthermore, with the strongest dependence on orbital period, the tidal ellipsoidal distortion component is exceptionally prominent in very short period systems such as TOI-2109 b with a period of 0.68 days (Wong et al., 2021a). In fact, for massive planets with ultra-short periods, such as WASP-18 b, tidal ellipsoidal distortion can be one of the most significant phase curve components (see Figure 1.8).

1.2.3 Doppler Beaming

Much like tidal ellipsoidal distortion, the Doppler beaming effect results directly from gravitational interactions between a star and a massive companion.

Each body orbits the centre of mass in a system. As highlighted in Chapter 1.1.2, large, short-period planets cause this centre of mass to deviate from the centre of the star such that it appears to wobble. As the star orbits this centre of mass, the observed photometric light is shifted slightly redward or blueward in wavelength depending on the motion of the star. These shifts in wavelength cause the peak of emission to periodically drift into and away from the finite wavelength band in which the system is being observed, resulting in overall variations in the level of light detected. The observed flux of the system is modulated by the rela-

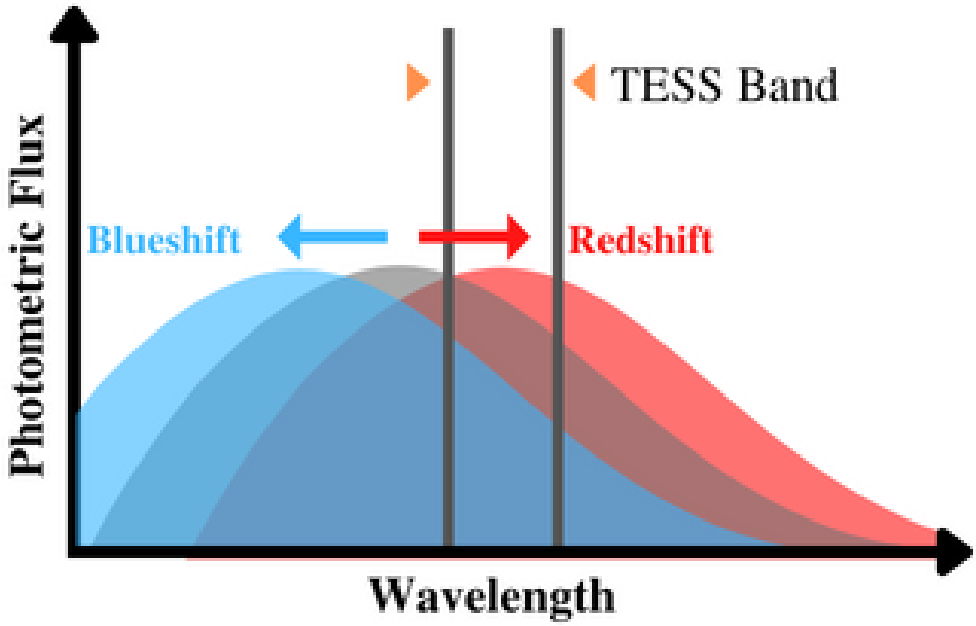

Figure 1.7: Schematic representation of the Doppler beaming effect with red- and blue-shifted spectral energy distributions for a star moving away or towards an observer respectively. When the spectra is red-shifted, the peak of emission is moved towards the TESS band and the star appears brighter. Conversely, the opposite effect is true for a blue-shifted spectrum.

tive radial velocity between the star and the observer. A schematic illustrating the shifts in wavelength and resulting level of light within the observing band is shown in Figure 1.7.

The amplitude of this modulation effect can be calculated from the system parameters (Shporer, 2017):

$$A_{beam} = 2.7\alpha_{beam}\left(\frac{P}{day}\right)^{-1/3} \times \left(\frac{\mathrm{M}_*}{M_\odot}\right)^{-2/3}\left(\frac{\mathrm{M}_p \sin i}{M_J}\right) ppm, \tag{1.7}$$

where the α_{beam} coefficient relates the stellar spectral distribution to the observed wavelength band. Approximating the star as a blackbody emitter, α_{beam} can be calculated at a specific frequency, ν, with the following equation:

$$\alpha_{beam,\nu} = \frac{1}{4}\frac{xe^x}{e^x - 1}, \text{ where } x \equiv \frac{h\nu}{kT_{eff}} \tag{1.8}$$

h is the Planck's constant and k is the Boltzmann constant. α_{beam} can then be calculated by integrating $\alpha_{beam,\nu}$ across the observable wavelength band (Shporer, 2017).

Of the three components, it is evident that the Doppler beaming effect is least heavily dependent on period. At shorter periods, this subtle effect can be dwarfed by other phase curve components. However, at longer periods the effects of atmospheric modulation and tidal ellipsoidal distortion begin to fall away more steeply, and only Doppler beaming remains (see Chapter 1.2.4).

As one might expect for a gravitational effect, Doppler beaming depends on both the stellar and planetary masses. Again, the effect is most prominent for systems with a high ratio of planetary to stellar masses.

By far the most subtle phase curve component for short period planets, Doppler beaming is often hard to measure for even the most massive planetary companions (Shporer, 2017). For ultra-short period hot Jupiters, Doppler beaming signals are often on the scale of 1-10 ppm (Loeb and Gaudi, 2003).

The shape of the orbital flux modulation induced by the beaming effect is identical to that of a radial velocity curve. However, radial velocity is defined to be positive when the object is moving away from the observer, but this corresponds to a decrease in measured flux due to the Doppler beaming effect for a typical stellar spectral energy distribution and optical observing band.

An alternative method to calculate the Doppler beaming contribution is shown in Equation 1.9, where A_{beam} is dependent on the radial velocity semi-amplitude, K (Shporer, 2017).

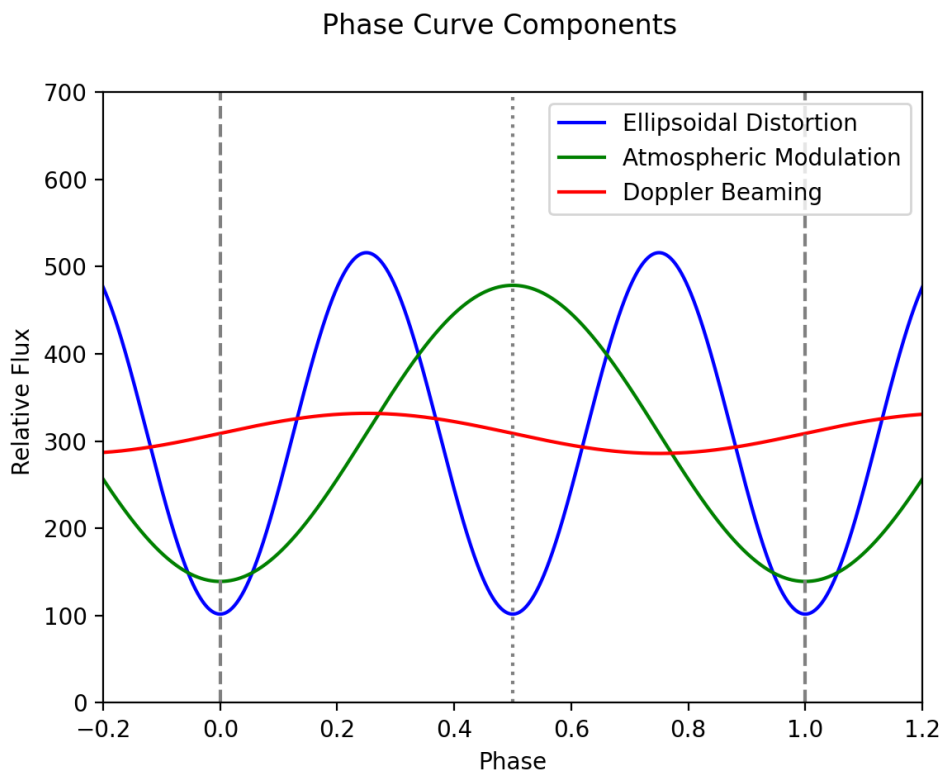

Figure 1.8: 3 major phase curve components for the known transiting planet WASP-18 b. WASP-18 b is 10.4 M_J hot Jupiter on on 0.94 day orbit around a star with a *TESS* magnitude of 8.8 (Shporer et al., 2019). The three components are tidal ellipsoidal distortion (blue), atmospheric modulation (green), Doppler beaming (red).

$$A_{beam} = 4\alpha_{beam}\frac{K}{c}, \tag{1.9}$$

where c is the speed of light in a vacuum. This equation demonstrates the intrinsic relationship between the Doppler beaming effect and the radial velocity motion of each system.

1.2.4 Combined Three-Component Model

Each of the three components is sinusoidal in shape, with varying amplitudes, periods and phase. Figure 1.8 illustrates these phase curve components for the known transiting planet WASP-18 b. WASP-18 b is a hot Jupiter with a mass of 9.8 M_J, and an orbital period of 0.94 days, resulting in one of the highest amplitude phase curve signals for a known planetary system (Hellier et al., 2009a; Shporer et al., 2019; Wong et al., 2020).

Planet	**WASP-18 b**
Tmag	8.83
$T_{\rm eff}$	6226 ± 140 K
R_*	1.35 ± 0.07 $R_\odot$
M_*	1.2 ± 0.17 $M_\odot$
Period	0.94 days
Inclination	84.4°
R_p	1.16 ± 0.06 R_J
M_p	10.4 ± 0.3 M_J

Table 1.1: System parameters for the known transiting planet WASP-18 b (Hellier et al., 2009a; Wong et al., 2020).

We use WASP-18 b as a case-study to examine the effect on the phase curve amplitude of varying planetary parameters. A complete set of system parameters for WASP-18 b is given in Table 1.1. These parameters are used to evaluate the total phase curve amplitude for varying angles of inclination, planetary masses, and orbital periods.

In the first instance, we set the planetary mass to reflect the true value for the system: $10.4\,M_J$. However, we allow the orbital inclination to vary from 90° to 45° in order to simulate non-transiting systems. Figure 1.9 demonstrates the change in amplitude for each of the three phase curve components as well as changes in the total amplitude. In total, across the 45° decrease, at a fixed orbital period of 0.94 days, we see a drop in amplitude of 115.3 ppm (41%).

With each decrease in inclination, there is a greater drop off in tidal ellipsoidal distortion than either of the other effects. This comes as a result of the effect's squared dependence on the inclination term (see Equation 1.5) and thus means that the tidal ellipsoidal distortion component is most prominent for high inclination or transiting systems.

We assume the distribution of orbital inclinations for non-transiting planets peaks at 60 °, and initially model all non-transiting planets at this inclination. As evident from Figure 1.9, the decrease in the total phase curve amplitude from transiting planets to those at 60° is less than 20%. Thus, the investigation on orbital inclination demonstrates that these phase curve components can be detectable not only for massive transiting planets but also for non-transiting hot Jupiters.

Next, we investigate the effect of changes in planetary mass to the total phase curve amplitude. As evidenced in Figure 1.8, WASP-18 b is an unusually massive planet; as such, the contribution of each phase curve component may not be typical for a larger sample of non-transiting planets. We set the angle of inclination to

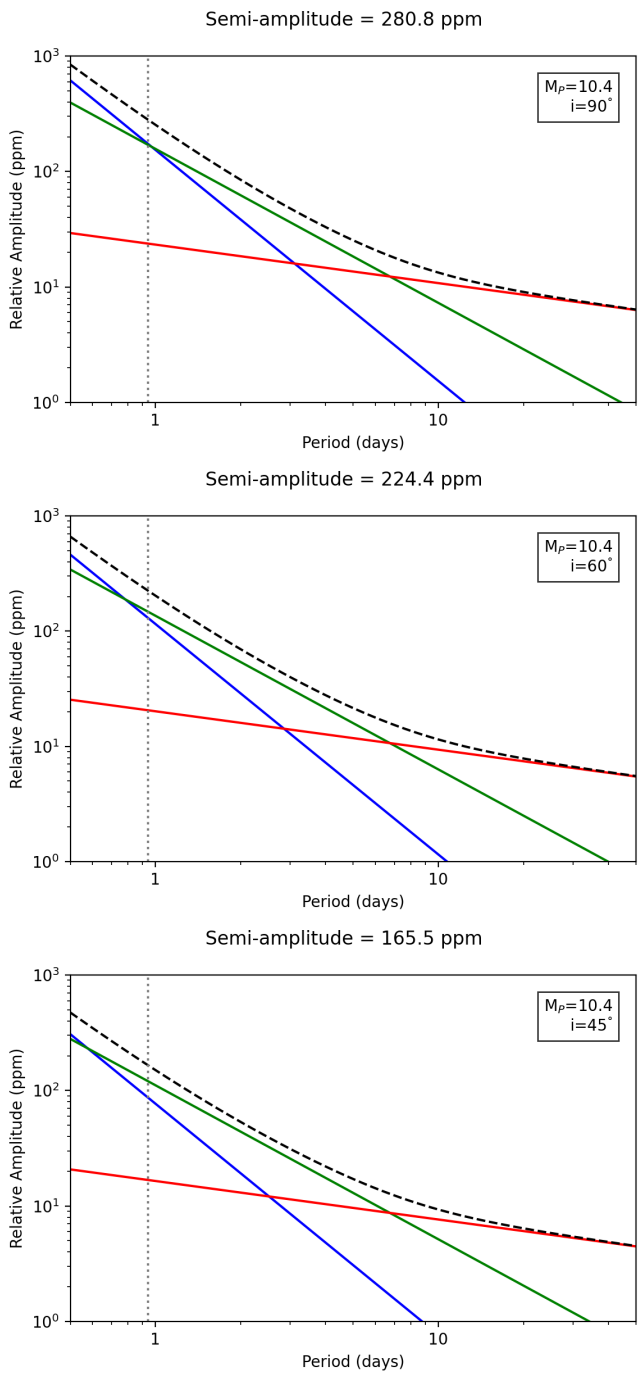

Figure 1.9: Relative amplitudes for the three phase curve components for a planet with similar properties to WASP-18 b with varying orbital periods and angles of inclination. The three phase curve components are: atmospheric modulation (green), tidal ellipsoidal distortion (blue), and Doppler beaming (red). The total phase curve amplitude is shown by the dashed black line, and the vertical dotted grey line illustrates the true period of the system: 0.94 days.

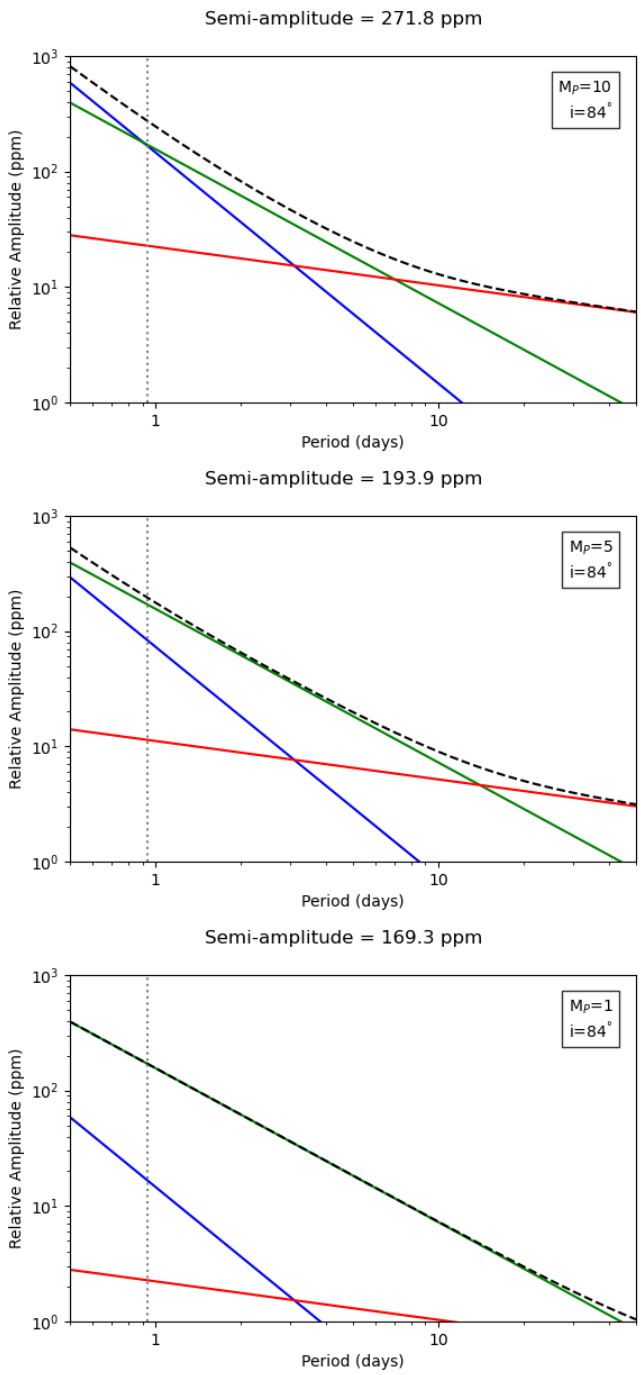

Figure 1.10: Relative amplitudes for the three phase curve components of the known transiting planet WASP-18 b with varying orbital periods and planetary masses. The line representations in this figure are the same as for Figure 1.9.

the true value of 84°and vary the true planetary mass from 1 to 10 M_J in order to investigate this effect. Figure 1.10 demonstrates the changes in amplitude of the phase curve components for three sample masses: 1 M_J, 5 M_J, and 10 M_J.

For exceptionally massive, short-period planets such as WASP-18 b, brown dwarfs such as KELT-1 b (Siverd et al., 2012; Wong et al., 2020), and even binary companions (Faigler and Mazeh, 2011), tidal ellipsoidal distortion is often the most significant phase curve component, greatly increasing the total phase curve amplitude. However, planetary companions with such high masses are incredibly rare (a fact masked by their natural affinity for detection) and thus we also consider systems with lower planetary masses.

For each of the three scenarios, the atmospheric modulation component is unchanged as the effect is not gravitationally induced and therefore does not depend on the planetary mass. However, tidal ellipsoidal distortion and Doppler beaming are both gravitational effects. As the mass decreases, these effects steeply drop off, such that for systems with planetary masses less than 5 M_J, the signal is often dominated by atmospheric modulation alone. For such systems, the total phase curve amplitude is often lower but can still be detectable, particularly at short periods.

For the purpose of this project, we consider only very short period, massive planets most likely to induce high amplitude phase curve signals. We label these planets as ultra-short period hot Jupiters and define them as those with orbital periods less than 2 days and masses between 0.5 and 13 M_J. These limits ensure the sample planets are hot, gaseous, and below the deuterium burning limit (Spiegel et al., 2011).

1.3 The Transiting Exoplanet Survey Satellite

The Transiting Exoplanet Survey Satellite (*TESS*; Ricker et al., 2015) mission was launched by NASA in April 2018 with the aim of creating an all-sky photometric survey to search for transiting planets around bright, nearby stars. *TESS* was specifically designed to capture signals of low-radius exoplanets ($R_p < 0.5\,R_J$). However, the telescope also excels at detecting and monitoring hot Jupiter planets, such as TOI-2109 b which was first discovered in 2021 by Wong et al. (2021a).

Shown in Figure 1.11, the *TESS* spacecraft has four identical wide-field cameras aligned vertically to create a field of view (FoV) that is 24°× 96° in size (Ricker et al., 2015). The four cameras are housed in a drum-like casing attached to the face of the telescope with two solar panel wings attached to the body. The spacecraft

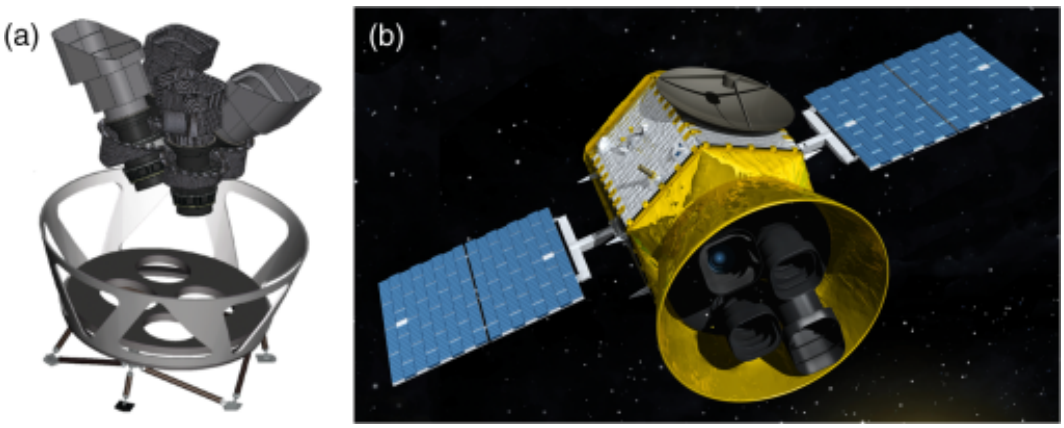

Figure 1.11: (a) Orientation of the four *TESS* cameras and mounting system (b) Artist impression of the *TESS* spacecraft (Ricker et al., 2015).

was placed into a highly elliptical 13.7-day orbit around the Earth.

In the first two years of the mission, *TESS* splits the sky into 26 sectors - thirteen sectors in each ecliptic hemisphere. These overlapping sectors each correspond to a region equal to the instantaneous FoV and provide near-complete coverage of the sky. Each sector consists of two spacecraft orbits (27.4 days) with a small interruption between them in which data is downloaded to the Earth. For the duration of a sector, the long axis of the FoV is oriented along a line of constant ecliptic longitude with Camera 4 centred on one of the ecliptic poles. At the end of the sector, the FoV is rotated by 27°and *TESS* begins observations of a new sector (Ricker et al., 2015; Jenkins et al., 2016).

Each of *TESS*'s four cameras consists of four charge coupled devices (CCDs) that are focused on a red-optical wavelength band from 600-1000 nm. The CCD array is read out at 2-second intervals with individual frames compiled at 2-minute cadence. In Years 1 and 2, full-frame images (FFIs) are compiled at 30-minute cadence. In Year 3, the cadence for FFIs was reduced to 10 minutes.

The individual frames are broken down into postage stamps that are roughly centred on a target star. From these postage stamps, individual pixels are selected for photometry such that the maximum amount of light from the target star is detected without including light from contaminating sources. These target pixels are called the aperture. The fraction of flux in the aperture from the target source is called CROWDSAP and at optimum returns a value of 1. Figure 1.12 shows the *TESS* postage stamp and target pixels for an example system.

The target pixels are used to extract light-curves from the FFIs with the Science Processing Operations Centre pipeline (SPOC; Jenkins et al., 2016). The

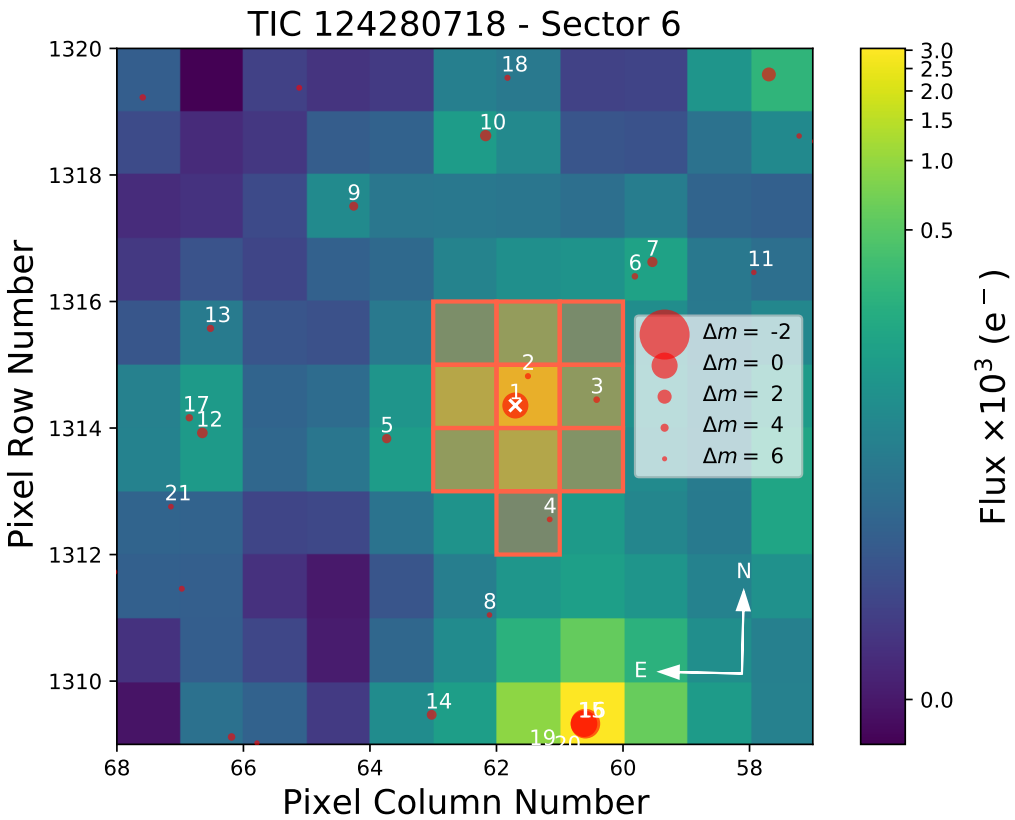

Figure 1.12: Target pixel files for the planetary candidate system TIC 124280718 from Sector 6. The red circles indicate sources from the Gaia DR2 catalogue that fall within the field. Each source has an associated *Gaia* magnitude scaled to the target (see legend). Each pixel represents 21 arcsec of space and is coloured based on the flux of electrons detected. The plot was created with the tpfplotter code, publicly available on GitHub.

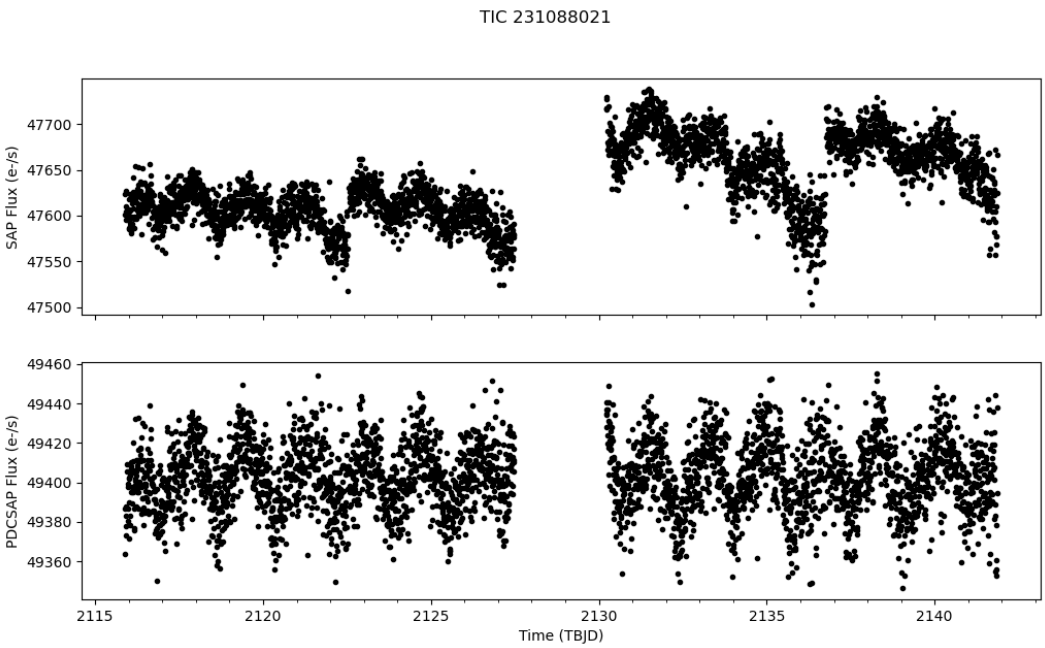

Figure 1.13: Comparison of the SAP (top panel) and PDC (bottom panel) light-curves for TIC 231088021 in Sector 33 with *TESS*.

SPOC pipeline produces two types of light curves: simple aperture photometry (SAP) and pre-search data conditioning (PDCSAP) light curves (Stumpe et al., 2012, 2014; Smith et al., 2012). The PDCSAP light curves are detrended for instrumental systematics and corrected for flux contamination from nearby, bright stars. Figure 1.13 shows both SAP and PDCSAP light-curves for an example system with a clear distinction between the simple and detrended data.

FFI light-curves are generated for $\sim 160,000$ stars per sector (Stassun et al. (2019)). However, between sectors there is always some overlapping regions, and some stars are observed more than once. There are a total of 1,422,325 unique stars with full-frame SPOC PDCSAP light-curves across both Year 1 and Year 3 observations (in the southern ecliptic hemisphere). Each of these stars is given an automatically generated *TESS* Input Catalogue (TIC) number to be used for identification.

In Year 1 of the primary mission (from 25 July 2018 to 18 July 2019), *TESS* observed the southern ecliptic hemisphere. For each sector in Year 1, the boresight was pointed -54° in ecliptic latitude such that Camera 4 was centred on the southern ecliptic pole.

For the second year of the primary mission, *TESS* turned to the northern ecliptic hemisphere. The northern hemisphere, much like the south, was observed

in 13 sectors with a rotation of 27° between each sector. However, coverage of the northern hemisphere is far less complete than the southern hemisphere due to a shift in spacecraft pointing in Sectors 14-16 and 24-26. These shifts were executed in order to allow maximum coverage of the sky whilst avoiding excessive contamination by stray moonlight in Cameras 1 and 2.

In Year 3 (from 4 July 2020 to 24 June 2021 - the first year of the extended mission), *TESS* revisited the southern hemisphere. There was a small pointing rotation in Year 3 sectors about the ecliptic pole in order to cover gaps between the Year 1 sectors extending from the ecliptic region. In this project we focus only on data from Year 1 and Year 3 of the mission. Figure 1.14 shows the placement of the FoV for each sector in Years 1 and 3 of the *TESS* mission.

Resulting from the sector rotation mechanics, regions near the southern ecliptic pole appear under near-constant observation throughout both years, whereas most regions near the ecliptic are observed only once in the year. Some regions, which fall between gaps in sectors, are only observed in one year and, as such, do not have repeat observations at this time. A total of 184,664 stars with full frame SPOC PDCSAP light-curves did not have repeat observations in Year 3. Contrastingly, light-curves of 184,289 new stars were obtained.

1.4 Phase Curve Detections

Phase curve components have been detectable in transiting objects for quite some time. Faigler and Mazeh (2011) demonstrated the potential for phased photometric variation searches as method a of detecting low-mass stellar companions with periods between 10 and 30 days. Furthermore, tidal ellipsoidal distortion and Doppler beaming were detected in *CoRoT* data (Auvergne et al., 2009) for the transiting brown dwarf *CoRoT-3b* (Mazeh and Faigler, 2010; Faigler, 2016).

The total amplitude of phase curve signals for hot Jupiters is typically only ∼100 ppm even for ultra-short period, giant planets (Wong et al., 2020, 2021b). To detect these variations requires extremely high precision photometry monitored over long time frames. Such data is generally only available from space-based photometric surveys such as *Kepler* (Borucki et al., 2010) or *TESS*.

The detection of phased photometric variations in *Kepler* (Borucki et al., 2010) data has been used to discover the transiting hot Jupiter Kepler-76b (Faigler et al., 2013), as well as to detect super-rotation in four transiting exoplanet systems (Faigler and Mazeh, 2015). Tidal ellipsoidal distortion was also detected in *Kepler* data for the transiting exoplanet HATS-P-7b (Welsh et al., 2010).

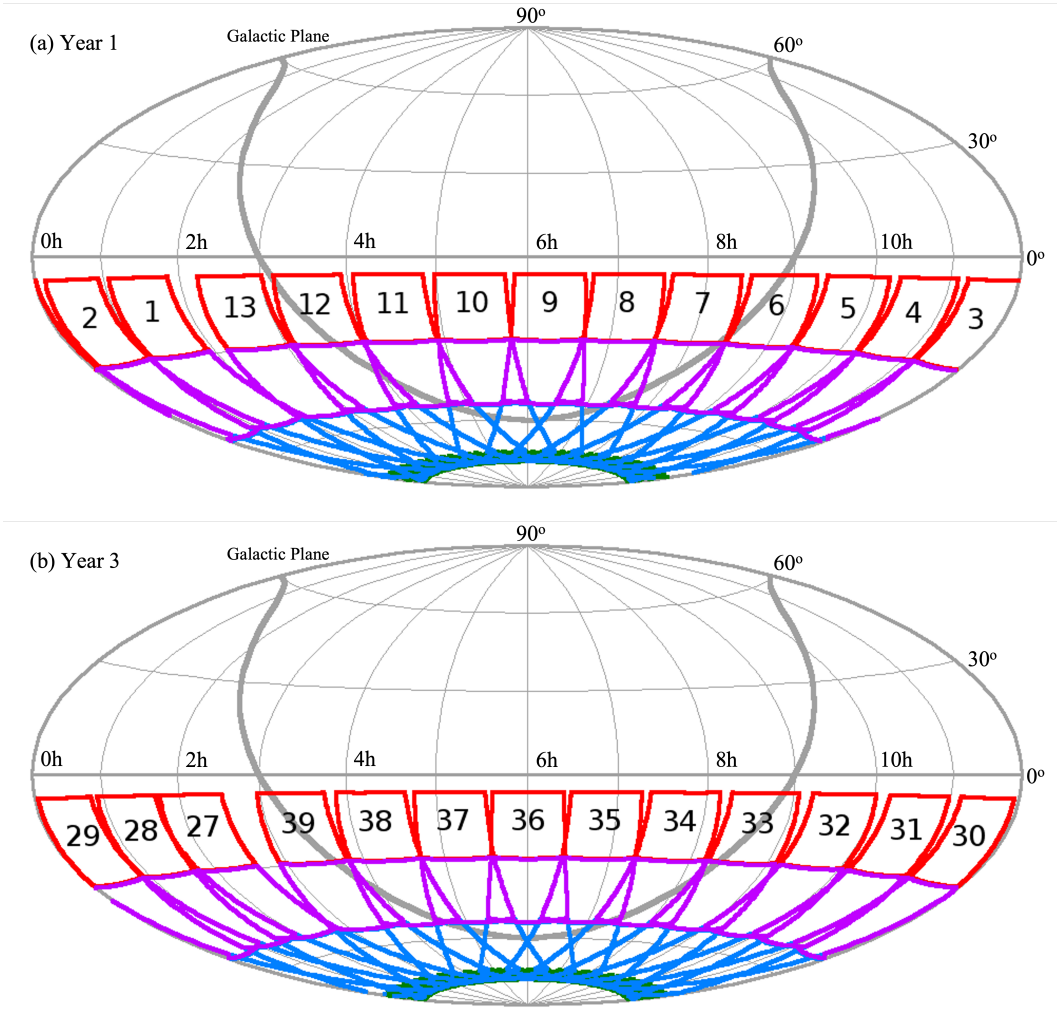

Figure 1.14: *TESS* sectors from years 1 and 3 of the mission. (a) *TESS* Sectors 1-13 observed in Year 1 of the mission from 25 July 2018 to 18 July 2019. (b) *TESS* Sectors 27-39 observed in Year 3 of the mission from 4 July 2020 to 24 June 2021. The thick grey line running through several sectors represents the galactic plane and the horizontal grey line represents the ecliptic plane. Image credit: TESS Observations, MIT.

Millholland and Laughlin (2017) attempted to detect non-transiting planets from the *Kepler* data set using phased photometric variations with a machine learning approach, identifying 60 high probability candidates. Ten of these candidates have since been followed up with radial velocity measurements, and three of these are now confirmed exoplanets (Lillo-Box et al., 2021).

Unlike its predecessor, *TESS* targets some of the brightest stars in the sky. As a result, there are various methods of planet confirmation and data collection for each of the target stars that were not available for many of the *Kepler* stars. These include access to data from the *Gaia* mission (Gaia Collaboration et al., 2016), the opportunity to obtain atmospheric observations, and a greater potential for radial velocity measurements.

Optical phase curves have been studied for at least 15 known transiting planets with *TESS*. With the completion of Year 1 in July 2019, Wong et al. (2020) began a study of phase curve components for known hot Jupiters in the southern ecliptic hemisphere. Shortly after, the study was followed up by Wong et al. (2021b) with a review of phase curve components for transiting planets in Year 2 data. Of the 34 total systems studied, 13 systems displayed photometric variations associated with at least one phase curve effect. However, to date, no non-transiting exoplanets have been discovered with phased photometric variations from the *TESS* mission.

In this project, we aim to discover non-transiting hot Jupiters in the *TESS* data set with masses between 0.5 and $13\,\mathrm{M}_J$, radii between 0.5 and $2.0\,\mathrm{R}_J$, and periods between 0.5 and 2.0 days.

1.5 Yield Estimation

In Section 1.2.4, we investigated the contribution of three effects on phase curve signals for non-transiting planets and conclude that phased photometric variations should be detectable for ultra-short period, massive non-transiting planets. However, this investigation does not yield any information on how many non-transiting hot Jupiter planets we can expect to detect with phased photometric variations from *TESS*.

Figure 1.15 shows the calculated occurrence statistics for various planet categories from the *Kepler* mission with planetary radii obtained from the *Gaia* mission's (Gaia Collaboration et al., 2016) second data release, DR2 (Gaia Collaboration et al., 2018; Hsu et al., 2019). From these statistics, the probability of a system hosting a large planet with a short orbital period ($\mathrm{R}_p > 6R_\oplus \approx 0.5\mathrm{R}_J$ and $P < 2$ days) is calculated to be $(0.18 \pm 0.12)\%$ (Hsu et al., 2019).

As mentioned in Chapter 1.3, the total number of unique stars with *TESS* FFI SPOC PDCSAP light-curves is 1,422,325. Logically this leads to a result of 2560 ± 1707 detectable hot Jupiters. However, not all *TESS* stars are amenable to planet detection through phased photometric variations:

- Light curves of bright stars have a better signal-to-noise ratio. Therefore, it is much easier to detect small-amplitude phased photometric variation signals in stars with a TESS magnitude < 11.
- Hot stars, with effective temperatures greater than 7200 K, often have other effects visible in their light-curves that can make it difficult to detect phased photometric variations. These effects include pulsations and instabilities.
- Giant stars ($R_* > 2R_\odot$) often show photometric variability that can mimic or mask phased photometric variation signals.
- Light curves with high levels of crowding (CROWDSAP< 0.9) include a large fraction of light in the aperture that is not from the target source. Low amplitude signals in these systems are unreliable and could be the result of blending.

Taking account of these restrictions, a sample of 141,762 stars with SPOC FFIs from *TESS* Years 1 and 3 is obtained. With this sample of stars, we can expect a total of 255 ± 170 planets to be detectable with phased photometric variations from the *TESS* southern ecliptic hemisphere, of which, 213 ± 154 will be non-transiting.

We use this yield estimation to motivate a search of 140,000 cool, bright, isolated dwarf stars for non-transiting planets via *TESS* phase curves. In the following chapter we set out the detailed methodology and results of this work.

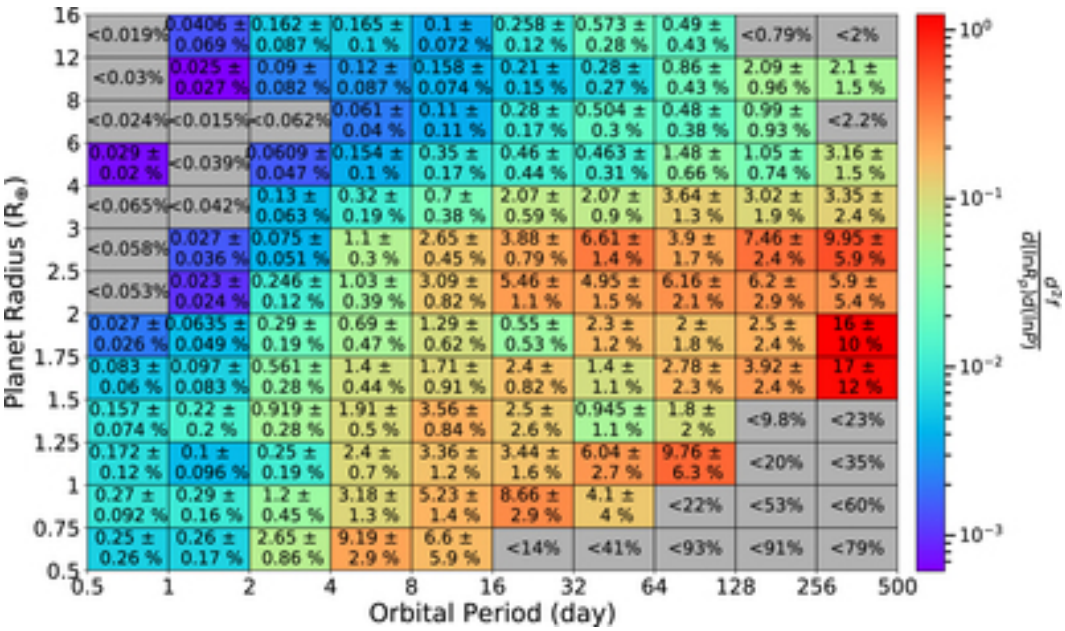

Figure 1.15: Occurrence statistics of various planets from the *Kepler* mission with planetary radii obtained from the *GAIA* mission's second data release, *DR2* (Hsu et al., 2019).

Chapter 2

A Search for Non-Transiting Exoplanets with Optical Light Phase Curves from TESS

This Chapter forms the basis of a draft paper that will be submitted to MNRAS for publication.

2.1 Introduction

Discovering exoplanets remains a major challenge in modern observational astronomy. To date, the majority of known exoplanets (77%) have been discovered via photometric transits[1] (Akeson et al., 2013). These include wide-field ground based transit surveys such as *WASP* (Pollacco et al., 2006), *HAT* (Bakos et al., 2004), *KELT* (Pepper et al., 2007), *HAT-South* (Bakos et al., 2013), and *NGTS* (Wheatley et al., 2018) as well as space-based surveys such as *CoRoT* (Auvergne et al., 2009), *Kepler* (Borucki et al., 2010), K2 (Howell et al., 2014) and *TESS* (Ricker et al., 2015).

Identifying exoplanets via photometric transits will only allow us to discover a small fraction of the true exoplanet population as it relies on a specific geometric alignment whereby the exoplanet passes in front of the host star from the observers point of view (Winn, 2010). For a hot Jupiter with a radius of 1.3 R_J transiting a solar-like star with a 2-day period, the geometric probability of a transit is 9.4%. This means that we would exclude over 90% of such planets in our photometric transit surveys.

[1] `https://exoplanetarchive.ipac.caltech.edu/`

However non-transiting exoplanets induce a phased photometric variation in the light-curve of the host star (Faigler and Mazeh, 2011; Shporer, 2017). The three main contributors to exoplanet phased photometric variations are atmospheric modulation, tidal ellipsoidal distortion, and Doppler beaming effects.

Atmospheric modulation is an effect that is comprised of two processes: reflection of star-light from the planet's atmosphere, and thermal emission from the planet's atmosphere due to dayside heating. Shporer (2017) give an empirical approximation for the amplitude of atmospheric modulation as:

$$A_{atm} = 57\alpha_{atm} \sin i \times \left(\frac{\mathrm{M}_*}{M_\odot}\right)^{-2/3} \left(\frac{P}{day}\right)^{-4/3} \left(\frac{\mathrm{R}_p}{R_J},\right)^2 ppm \tag{2.1}$$

where M_* is the mass of the host star, R_p is the radius of the planet, P is the orbital period of the planet, and i is the inclination of the orbital plane of the of the planet. α_{atm} is an order of unity coefficient that depends on the efficiency of atmospheric heat redistribution and reflectivity. For most hot Jupiter planets, atmospheric modulation dominates the phase curve signal with amplitudes on the order of 100 ppm.

Tidal ellipsoidal distortion is a gravitational effect resulting from the interaction of two massive bodies such as a host star and a planetary companion. The planet exerts a gravitational force on the star, distorting it into an ellipsoidal shape along the star-planet axis. As a result, twice per orbit, an elongated side of the star is presented to the observer. The subsequent modulation in flux is approximated with the following equation (Shporer, 2017):

$$A_{ellip} = 13\alpha_{ellip} \sin i \times \left(\frac{\mathrm{R}_*}{R_\odot}\right)^3 \left(\frac{\mathrm{M}_*}{M_\odot}\right)^{-2} \left(\frac{P}{day}\right)^{-2} \left(\frac{M_p \sin i}{M_J}\right) ppm, \tag{2.2}$$

where M_p is the mass of the planet. α_{ellip} is a coefficient that accounts for the stellar limb darkening and gravity darkening of the host star.

Generally a more subtle effect, the amplitude of tidal ellipsoidal distortion is typically on the order of 10 ppm. However, it can contribute significantly for high mass companions such as WASP-18 b (Hellier et al., 2009b; Shporer et al., 2019; Wong et al., 2020) and KELT-1 b (Siverd et al., 2012; Wong et al., 2021b). Furthermore, due to a strong dependence on planet period, the effect is also more prominent in very short period systems such as TOI-2109 b with a period of 0.67 days (Wong et al., 2021a).

Doppler beaming is a subtle effect that accounts for photometric variation in the host star due to the radial velocity variations induced by the orbiting compan-

ion. As the star orbits the system centre of mass, its spectral energy distribution is shifted redward and blueward via the Doppler shift. This moves the spectral energy distribution with respect to the observers passband, and hence can lead to photometric variation. The amplitude of this modulation is approximated as (Shporer, 2017):

$$A_{beam} \approx 2.7\alpha_{beam}\left(\frac{P}{day}\right)^{-1/3} \times \left(\frac{\mathrm{M}_*}{M_\odot}\right)^{-2/3}\left(\frac{\mathrm{M}_p \sin i}{M_J}\right) ppm, \tag{2.3}$$

where the α_{beam} coefficient relates the stellar spectral distribution to the observers passband.

Doppler beaming is by far the most subtle of the three phase curve components for short period planets. With amplitudes often <10 ppm, Doppler beaming is hard to measure for even the most massive planetary companions (Shporer, 2017).

The total amplitude of the phased photometric variation from these three effects is typically only ∼100 ppm even for very short-period giant planets (Wong et al., 2020, 2021b). To detect such variation requires extremely high precision photometry monitored over long baselines. Such data is generally only available from space-based photometric surveys. Tidal ellipsoidal distortion and Doppler beaming were detected in CoRoT data for the transiting exoplanet/brown dwarf CoRoT-3 b (Mazeh and Faigler, 2010). Tidal ellipsoidal distortion was also detected using Kepler data for the transiting exoplanet HATS-P-7 b (Welsh et al., 2010). The detection of phased photometric variation in Kepler data has also been used to discover the transiting hot Jupiter Kepler-76 b (Faigler et al., 2013), as well as detect super-rotation in four transiting exoplanet systems (Faigler and Mazeh, 2015). More recently data from the Transiting Exoplanet Survey Satellite mission (*TESS*; Ricker et al., 2014) has been used to detect phased photometric variation in a number of known transiting hot Jupiter systems (Shporer et al., 2019; Wong et al., 2020, 2021b,a).

Discovering non-transiting exoplanets using phased photometric variation is attempted in Millholland and Laughlin (2017), with 60 candidates identified from the Kepler data. Ten of these candidates have been followed-up via radial velocity, with three now confirmed as exoplanets (Lillo-Box et al., 2021). To date, no discoveries have been made of non-transiting exoplanets using phased photometric variation from the *TESS* data. In this paper we attempt to make such discoveries.

In Section 2.2 we set out the *TESS* data and sample selection used for searching for phased photometric variation. In Section 2.3 we set out our detection pipeline

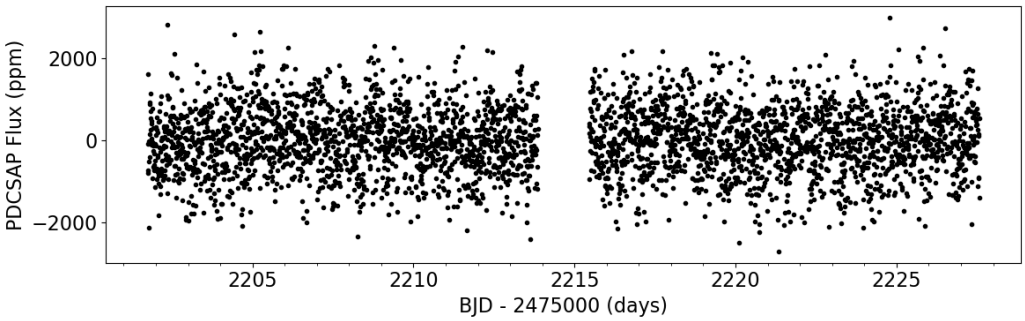

Figure 2.1: Example of a *TESS* 10-minute cadence, full-frame image light curve from the *TESS* SPOC pipeline for one of our candidates, TIC 124280718 (Sector 33). The PDCSAP flux has been normalised and instrumental effects have been removed to leave only real astrophysical variability in the light-curve. A data gap is visible in the middle of the Sector for a data downlink between each 13.7 day spacecraft orbit. This is a solar-type dwarf star (T_{eff}=5249 K) with a *TESS* magnitude of 10.94.

used for searching the *TESS* data. In Section 2.4 we set out the methods used to visually vet and model the candidate systems. In Section 2.5 we set out the results of our search. In Section 2.6 we discuss our candidates individually and look at their global properties. Finally, in Section 2.7 we set out our conclusions from this study.

2.2 Light-Curves

2.2.1 TESS Observations

The Transiting Exoplanet Survey Satellite (TESS; Ricker et al., 2015) is a wide-field space-based photometric mission designed to detect transiting exoplanets around bright, nearby stars. *TESS* operates at at a red-optical bandpass from 600-1000 nm using four identical wide-field cameras, with a combined field-of-view is $24° \times 96°$. In Year 1 of the *TESS* primary mission (from 25 July 2018 to 18 July 2019), *TESS* observed the southern ecliptic hemisphere over 13 sectors, each sector having a duration of approximately 27 days.

After observing the northern ecliptic hemisphere, *TESS* revisited the southern ecliptic hemisphere in Year 3 (4 July 2020 to 24 June 2021). As a result, observations of most stars were repeated. However, there was a small pointing rotation in Year 3 sectors about the ecliptic pole in order to cover gaps missed in Year 1.

TESS full-frame images (FFI) are sampled at a cadence of 30 mins for Year 1 and 10 mins for Year 3. These FFIs are processed into light-curves using the Science

Processing Operations Centre pipeline (SPOC; Jenkins et al., 2016). The SPOC pipeline produces two types of light-curves: simple aperture photometry (SAP) and pre-search data conditioning (PDCSAP) light-curves (Stumpe et al., 2012, 2014; Smith et al., 2012). The PDCSAP light-curves are detrended for common-mode instrumental systematics and corrected for flux contamination from nearby, bright stars (see example in Figure 2.1). We use the FFI SPOC PDCSAP light-curves for our search for phased photometric variation. For Year 1 and Year 3 light-curves, there are a total of 1,422,325 stars with full-frame SPOC PDCSAP light-curves (see Figure 2.2).

2.2.2 Sample Selection

We selected stars to search from the *TESS* FFI SPOC PDCSAP light-curves from the southern ecliptic fields using the following selections:

- *Stellar Magnitude (Tmag*< 11*):* In order to discover planets via their phased photometric variation effects, we need to search light-curves for signals with amplitudes on the order of 100 ppm. For *TESS* light-curves this means we are only sensitive to detecting these signals for bright stars.

- *Stellar Effective Temperature (*$T_{\rm eff} < 7200\,K$*):* Hot stars often show photometric variability due to pulsations, which can be confused with a phased photometric variation signal. Hot stars are also not good targets for radial velocity confirmation, since they have fewer sharp absorption lines and rotate faster than solar-type stars.

- *Stellar Radius (*$R_* < 2\,R_\odot$*):* Sub-giant and giant stars show photometric variability that may mimic or mask the phased photometric variation signal. Furthermore, sub-giant and giant stars are not favourable stars for radial velocity confirmation. In order to make this cut we use the stellar radius as estimated in the *TESS* Input Catalog Version 8 (TIC-8; Stassun et al., 2019).

- *Crowding (CROWDSAP > 0.9): TESS* photometry suffers from crowding issues due to large pixel size ($21\times21''\,{\rm pix}^{-1}$). To quantify this, SPOC calculates a crowding metric called CROWDSAP for each light curve, which is the fraction of flux in the aperture from the target star.

After applying these cuts we are left with a total of 141,762 stars (see the flowchart in Figure 2.2), which form the stellar sample used for our phased photometric variation search set out in Chapter 2.3. We retrieve these light curves from the Mikulski Archive for Space Telescopes (MAST) portal.

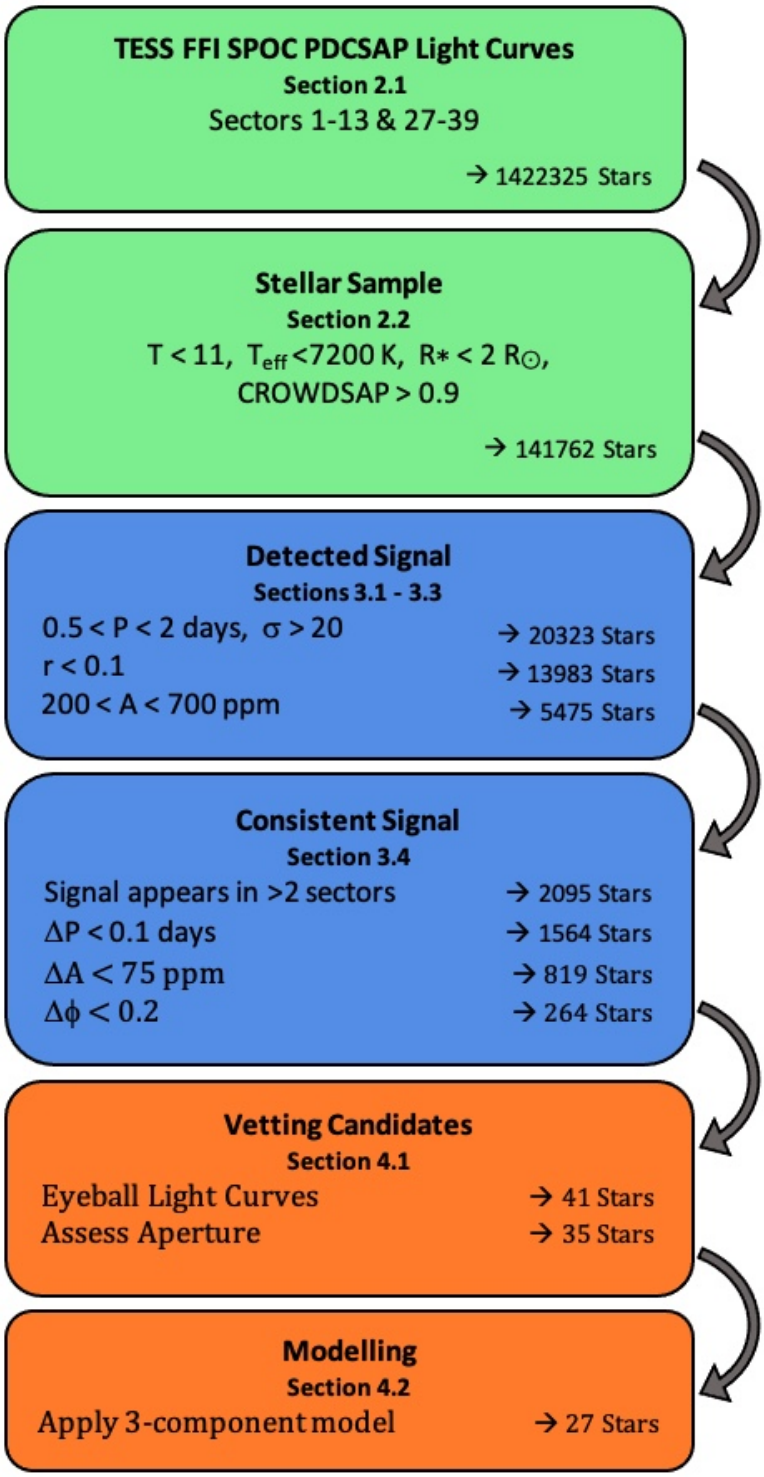

Figure 2.2: Flowchart outlining the steps of our phased photometric variation search of *TESS* FFI SPOC PDCSAP light curves from the southern ecliptic hemisphere. At each step we list the number of candidate systems remaining in the search.

2.3 Phased Photometric Variation Search

2.3.1 Identifying Periodic Variability

In order to detect non-transiting planets in the *TESS* data we need to detect low amplitude, short period signals similar to the out-of-transit variation detected for transiting planets with *TESS* (e.g. Wong et al., 2020, 2021b). We search our sample of selected *TESS* light-curves (Section 2.2.2) using the Lomb-Scargle algorithm (LS; Lomb, 1976; Scargle, 1982) as implemented in Millholland and Laughlin (2017). We run the LS algorithm over the period range 0.5-2.0 days, with a resolution of 40 samples per peak. The very short period range is selected since the expected amplitude for the phased photometric variation signal for each of the three primary components is strongly dependent on orbital period (see Equations 2.1, 2.2 and 2.3), and the *TESS* data is only sufficiently precise to detect very high amplitude signals. The window extends down to 0.5 days in order to capture the rare ultra-short period systems with very high amplitude phased photometric variation signals analogous to transiting planets WASP-18 b at 0.94 days (Hellier et al., 2009b; Shporer et al., 2019) and TOI-2109b at 0.67 days (Wong et al., 2021a).

We determine the LS significance at each period in the power spectrum by calculating the number of median absolute deviations between the LS power at each specific period and the global median. In our search for phased photometric variation we only select candidates with robust signals that have a peak LS significance greater than 20 absolute deviations from the global median to ensure the signals are real. We also found a large number of systems show variability at periods >2 days, which seemed to be due either to systematic noise (such as *TESS* momentum dumps or scattered light) or astrophysical effects (such as stellar rotation). In order to remove these false candidates we decided to focus only on the systems with periods <2 days. This dramatically reduced the size of the candidate list while preserving those short period systems for which we expect to find the phased photometric variation most robustly. Figure 2.3 is an example Lomb-Scargle significance periodogram for the previously referenced system TIC 124280718.

These cuts resulted in 5475 candidates remaining from the original 141,762 stars in our sample.

2.3.2 Removing Non-Sinusoidal Signals

Although the combination of effects that result in exoplanet induced phased photometric variation can result in many different signal shapes, the majority of systems will show a near-sinusoidal shape. By contrast, many other types of stellar variabil-

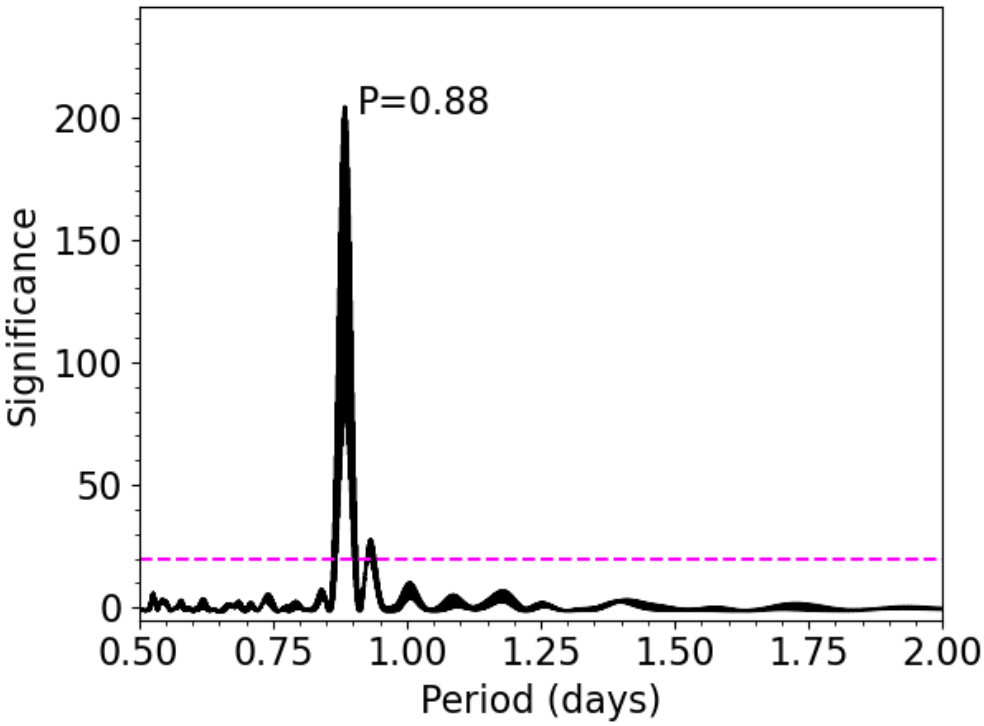

Figure 2.3: The Lomb-Scargle significance periodogram for candidate system TIC 124280718 from Sectors 6 and 33 evaluated over the period range from 0.5 to 2.0 days. The black solid line represents the LS significance, and the pink dashed line represents the significance threshold at $\sigma = 20$. For this example a significant period was detected at 0.88 days.

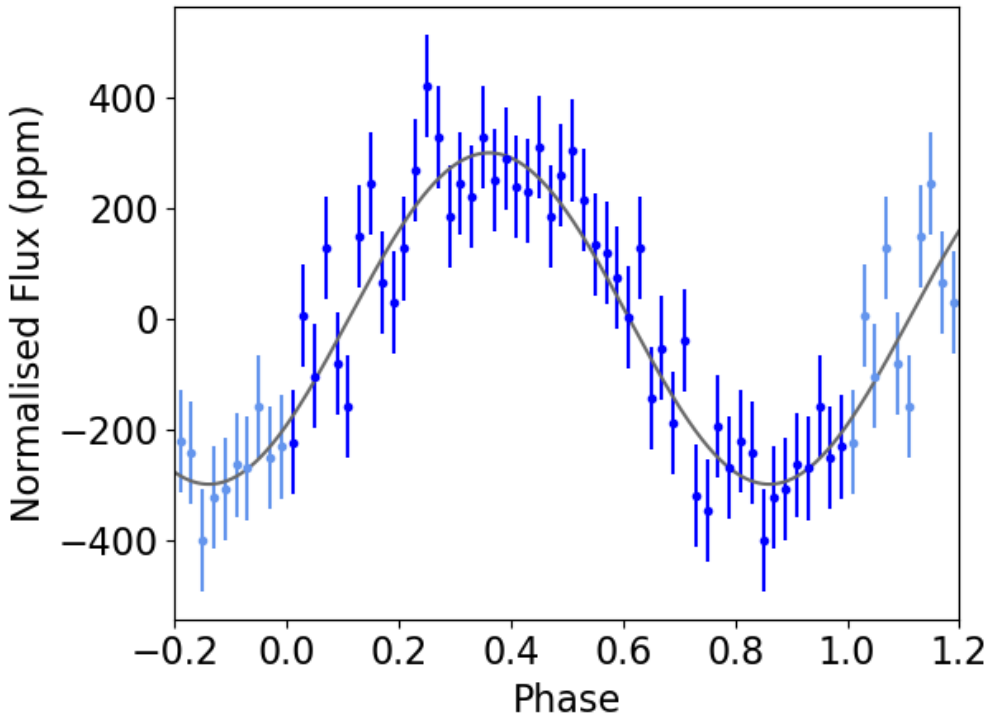

Figure 2.4: Example of a phase-folded, binned light curve for candidate system TIC 124280718. The light curve has been phase-folded at a period of 0.88 days (extracted from the Lomb-Scargle periodogram in Figure 2.3) and binned in phase to 50 points. Repeated data points are shown in light blue for continuity. The best fit sinusoidal curve is plotted in grey with a semi-amplitude of 287 ppm.

ity or systematic noise can be non-sinusoidal. Therefore by selecting only candidates with near-sinusoidal signals we can remove a large number of false positive light-curves.

We fold each of the candidate light-curves at the period corresponding to their peak LS significance. We then fit a sinusoidal function to the phase-folded light-curve using a non-linear least-squares fitting algorithm allowing the amplitude, phase and flux-offset to vary. The period is fixed to the peak period determined by the LS significance from Section 2.3. An example of such a fit is show in Figure 2.4.

We calculate the associated least-squares regression value for each system from the covariance of the data and the sinusoidal fit. We only select candidates that have a regression value of <0.1, which removes any candidates that display significantly non-sinusoidal variability.

Name	**Tmag (mag)**	**$T_{\rm eff}$ (K)**	**P (days)**	**R_p (R_J)**	**M_p (M_J)**	**A (ppm)**	**Citations**
WASP-12 b	11.1	6154	1.09	1.79	1.47	267	Hebb et al. (2009); Wong et al. (2021b)
WASP-18 b	8.8	6226	0.94	1.16	9.80	293	Hellier et al. (2009b); Shporer et al. (2019); Wong et al. (2020)
WASP-121 b	10.2	6776	1.27	1.76	1.16	214	Delrez et al. (2016); Wong et al. (2020)
KELT-1 b	10.2	6596	1.22	1.08	27.23	530	Siverd et al. (2012); Wong et al. (2021b)
KELT-13A b	10.3	7081	1.76	1.45	8.00	156	Temple et al. (2017); Wong et al. (2021b)
KELT-16 b	11.4	6430	0.97	1.45	2.75	189	Oberst et al. (2017); Wong et al. (2021b)
TOI-2109 b	9.8	6647	0.67	1.35	5.02	458	Wong et al. (2021a)

Table 2.1: Seven known transiting hot Jupiter planets with phased photometric variations detected in *TESS*.

2.3.3 Amplitude Selection

In order to focus only on exoplanet induced phased photometric variation, we need to select only candidates where the signal could reasonably be expected to originate from orbiting gas giant exoplanets. Fortunately we have a very clean sample of such systems in the form of the known transiting hot Jupiters monitored by *TESS* (Wong et al., 2020, 2021b). From this sample, we are able to identify seven systems with periods <2 days and approximately similar *TESS*-band magnitudes to our sample. We list these systems in Table 2.1. From these seven systems we determined that the most likely amplitude of phased photometric variation for non-transiting hot Jupiters in our sample would be in the range of 200-700 ppm.

We therefore selected only candidates with sinusoidal signal amplitudes of between 200-700 ppm in a single *TESS* sector. This removed a number of candidates that were of high amplitude, in particular the short period eclipsing and non-eclipsing binary stars in our candidate list.

2.3.4 Identifying Consistent Signals

Over extended periods of time, planetary phase curves should remain stable in amplitude and phase in comparison with most other stellar or instrumental light curve variability, which may change with time (Millholland and Laughlin, 2017). With this in mind, we tested if our candidates kept a constant phased photometric variation signal between multiple *TESS* sectors.

We require our candidates to have been observed in two or more *TESS* sectors. This reduced the number of candidates down to 2095. We then require the peak LS significance for those sectors to match to within a period of 0.1 days, which leaves us with 1564 candidates. We also require the amplitude for each sector to match within 75 ppm, and this leaves us with 819 candidates. Finally, we require the phase to match within 20 %. This generous phase matching allows for the fact that our candidates have short period orbits, so a small error in the period would compound to a large phase error between Year 1 and Year 3 observations. After this phase matching we are left with a total of 264 phased photometric variation candidates. The number of remaining candidate systems after each step is set out in Figure 2.2. The remaining candidates were visually inspected as set out in Section 2.4.

2.4 Candidate Vetting

2.4.1 Visual Inspection

We conducted a visual inspection of all 264 candidates from our phased photometric variation search set out in Section 2.3.

We assessed each candidate by inspecting the SPOC PDCSAP light-curves plotted both in time and phase. In particular we looked at amplitude variations over a given sector, which would not be expected from a real exoplanet phased photometric variation signal. We also looked for any unusual features in the shape of the phase-folded light-curves or in the LS significance power spectra. Candidate systems were ranked depending on the number of these characteristics present in the data. Systems showing strong signs of one or more of the above characteristics were deemed to be false positives, and removed from the candidate list. 41 systems displayed none of the characteristics and were deemed to be good candidates.

2.4.2 Neighbouring Stars

Shallow periodic photometric variations can easily be caused by neighbouring variable stars that blend some fraction of their light into the TESS aperture. To check for this, we inspected the TESS pixel level data of our 41 candidate stars. For six of our candidates we found some evidence that the detected photometric signal may have originated from a neighbouring star. We therefore deemed these to be false positives and removed them from our candidate list. This left us with 35 candidate systems, which we then fitted with a three-component model as set out below in Section 2.4.3.

2.4.3 Three-Component Model

The final step in our vetting involved fitting a three-component model to each candidate light-curve that would account for the three primary phased photometric variation effects set out in Chapter 2.1, namely atmospheric modulation, tidal ellipsoidal distortion, and Doppler beaming.

We began by recalculating a period by applying a LS periodogram to the combined, normalised data from all available *TESS* sectors for a given candidate. We then phase-folded the *TESS* data for each candidate on the best LS period. With the phase-folded data, we then simultaneously fit for atmospheric modulation, tidal ellipsoidal distortion, and Doppler beaming using Equations 2.1, 2.2, and 2.3, respectively.

For each candidate system, the stellar mass and radius are obtained from TIC-8 (Stassun et al., 2019). The planetary mass and radius are both parameters obtained from the 3-component model fit. The angle of orbital inclination, i, is set to a median value of 60° for all candidates.

α_{atm} is estimated for each system using our knowledge of atmospheres from known transiting planets from Wong et al. (2020), Wong et al. (2021b), Shporer et al. (2019) and Wong et al. (2021a). We selected three planets that were representative of the population: WASP-100 b (Hellier et al., 2014), WASP-18 b (Hellier et al., 2009b), and KELT-13A b (Temple et al., 2017). These planets were used as a guide for α_{atm} values for the candidate planets. A value for the equilibrium temperature of each candidate system was calculated. Based on this equilibrium temperature, the system was matched to one of the three selected exoplanets. The value of α_{atm} used for the model fitting was taken from the matched system except where this did not provide a suitable model fit. In these cases, the α_{atm} value was matched to a system with a higher value. Three candidate systems could not be suitably modelled by the known exoplanets. These systems are highlighted in Section 2.5.3. The value of α_{atm} used for each candidate system is shown in Table 2.2.

The effects on α_{ellip} of changes in gravity and limb darkening are relatively subtle. We assume each of our candidate stars to be similar and as such, we set the gravity and limb darkening coefficients to $g = 0.28$ and $u = 0.54$, respectively (Claret and Bloemen, 2011). Thus, for all candidate systems, $\alpha_{ellip} = 1.21$. We note that the value of this parameter is not critical to the model fit.

The α_{beam} coefficient accounts for differences in the wavelength of the observing band and the peak distribution of emitted light. Assuming the emission acts as a black body, α_{beam} is therefore dependent on the stellar effective temperature and the wavelength of the observing band. Similar to atmospheric modulation, α_{beam} is estimated for each system using knowledge of known planetary systems. However, as a much more subtle effect, α_{beam} is calculated using a single average of values for known transiting systems with *TESS* (Wong et al., 2020, 2021b,a). These systems are set out in Table 2.1. The value of α_{beam} used for all candidate systems is 0.73.

Unlike for transiting exoplanet candidates, the orbital inclination for our non-transiting candidates is unknown. We therefore assume an inclination of $i = 60°$ for all candidates. We also assume that all candidates are in circular orbits, which is a good assumption given that we would expect such short period planets to be tidally circularised on a short timescale (Mazeh, 2008).

We apply a 3-component model to each candidate with fixed α coefficients, orbital inclinations and stellar parameters for each system. A least-squares fit allows

only the phase, flux offset, and planetary parameters to vary. The planetary mass is fitted between the boundaries of 0.5 and $13\,\mathrm{M}_J$ with an initial estimate of $4\,\mathrm{M}_J$. The boundaries for the planetary radius are $0.5\,\mathrm{R}_J$ and $2.0\,\mathrm{R}_J$ with an initial estimate of $1.3\,\mathrm{R}_J$.

After calculating the three model components, we assess each of the 35 candidate systems individually to establish whether the model is an appropriate fit. We analyse the residuals for each system, ensuring they are evenly scattered and approximately random. At this stage, 8 systems were considered to have shapes that were inconsistent with the model and were disregarded. These systems are most likely to be variable stars with near-sinusoidal variation.

Thus our final candidate list consists of 27 systems, each of which passed all of our vetting checks. The three-component model fits for these candidates are plotted in Section 2.7. We discuss these candidates in Section 2.5 below.

2.5 Results

Our search and vetting of the stellar sample set out in Sections 2.3 and 2.4 results in a total of 27 phased photometric variation candidates which are set out in Table 2.2. Table 2.2 contains the best fit amplitudes for each of the three components in the phased photometric variation fit, as well as the stellar properties and estimated planet radius, planet mass, and orbital period. We also tabulate the expected radial velocity semi-amplitude ($K\sin(i)$), which is useful for planning for follow-up spectroscopic observations.

The phase-folded light curves for each of the 27 candidates, along with the best fitting three-component models, are plotted in Figures 2.7- 2.33.

TIC ID	**Sectors**	$Tmag$ **(mag)**	$\mathbf{T}_{\mathrm{eff}}$ **(K)**	R_* $(R_\odot)$	M_* $(M_\odot)$	α_{atm}	A_{atm} **(ppm)**	A_{ellip} **(ppm)**	A_{beam} **(ppm)**	A **(ppm)**	P **(days)**	$\mathbf{R}_p$ $(\mathbf{R}_J)$	$\mathbf{M}_p$ $(\mathbf{M}_J)$	$K\sin(i)$ $(\mathbf{m\,s^{-1}})$
124280718	6, 33	10.9	5249	0.91	0.90	1.66	299.8	26.0	3.5	299.9	0.88	1.70	1.83	417
141372241	8, 9	9.3	5784	0.84	1.04	1.66	223.7	<3.0	<0.8	223.7	1.04	1.72	<0.5	98
266784171	3, 30	9.9	5984	0.97	1.10	3.61	266.1	<1.2	<0.6	266.1	1.93	1.96	<0.5	76
351601347	13, 27	10.4	6044	1.88	1.12	3.61	204.6	<25.6	<0.8	204.6	1.11	1.19	<0.5	91
243494729	11, 38	10.3	6352	1.51	1.26	3.61	258.0	30.7	3.7	258.1	1.56	1.75	2.90	435
100512121	5, 6, 32, 33	9.6	6443	1.45	1.30	3.61	134.8	<19.0	<0.8	134.8	0.75	0.78	<0.5	94
362086194	11, 12, 13, 27, 38, 39	10.8	6522	1.51	1.34	2.49	52.3	64.3	4.8	95.5	1.12	0.77	3.54	569
62078858	7, 34	10.9	6547	1.80	1.35	3.61	238.3	<34.3	<0.8	238.3	0.74	1.05	<0.5	92
96918158	6, 7, 33, 34	10.8	6660	1.47	1.40	2.49	202.2	34.6	4.1	202.3	1.35	1.75	3.30	484
251855019	2, 29	10.6	6677	1.81	1.41	3.61	242.4	28.7	1.5	242.4	1.18	1.46	1.13	173
200526405	6, 32	10.9	6762	1.76	1.45	3.61	204.7	<4.5	<0.5	204.7	1.86	1.83	<0.5	64
2758451	2, 29	10.3	6804	1.68	1.46	3.61	303.6	13.5	0.7	303.6	1.0	1.49	0.52	82
196322336	8, 34, 35	10.3	6828	1.47	1.47	3.61	268.1	<13.2	<0.7	268.1	0.81	1.21	<0.5	84
264903281	7, 34	10.8	6830	1.88	1.47	3.61	335.5	29.5	0.9	335.5	0.90	1.45	0.65	106
174001896	7, 8	9.8	6832	1.74	1.48	7.22	306.5	20.9	2.7	306.5	1.85	1.59	2.49	317
258914469	11, 37	10.6	6842	1.98	1.48	3.61	326.4	<12.0	<0.6	326.4	1.32	1.86	<0.5	71
121026156	4, 31	10.1	6848	1.85	1.48	3.61	250.7	<14.7	<0.6	250.7	1.08	1.42	<0.5	76
380914081	13, 39	10.0	6853	1.56	1.48	3.61	329.2	<8.6	<0.6	329.2	1.09	1.64	<0.5	76
56126064	5, 32	10.8	6877	1.78	1.49	7.22	470.5	25.4	2.9	470.5	1.77	1.92	2.63	338
235055610	4, 5, 6, 31, 32, 33	10.7	6890	1.67	1.50	2.49	83.1	54.0	8.5	107.4	1.9	1.44	7.97	997
454198279	05, 32	9.3	6940	1.51	1.52	3.61	394.2	<8.1	<0.6	394.2	1.04	1.76	<0.5	76
59534077	7, 8, 33, 34, 35	10.1	6992	1.49	1.54	3.61	210.9	<3.4	<0.6	210.9	1.56	1.69	<0.5	66
144305370	09, 36, 46	10.6	7019	1.61	1.55	3.61	212.7	<12.1	<0.7	212.7	0.92	1.20	<0.5	78
52199183	9, 36	10.8	7113	1.69	1.58	3.61	260.9	19.0	1.0	260.9	0.97	1.38	0.78	118
388496589	8, 9, 34, 35, 36	10.6	7128	1.43	1.59	3.61	184.8	<11.7	<0.7	184.8	0.76	0.99	<0.5	82
158716775	9, 10, 36	10.3	7163	1.54	1.60	2.49	124.2	<2.5	<0.5	124.2	1.83	1.75	<0.5	61
443857085	7, 34	10.7	7171	1.70	1.60	10.82	528.2	22.6	3.9	528.2	1.98	1.83	3.91	462

Table 2.2: Catalogue of 27 non-transiting hot Jupiter candidates.

2.5.1 Candidate Properties

The 27 phased photometric variation candidates range in brightness between values of 9.1<Tmag<10.9, with the distribution in Tmag set out in Figure 2.5 (a). The magnitude distribution of the candidates is weighted towards the faint end of our stellar sample, as expected given the underlying distribution is also weighted towards the fainter end. However, since our initial stellar sample cut was T<11, all of the candidates are bright stars and are suitable for high precision radial velocity follow-up.

The candidate host stars range in temperature from $5200<T_{\rm eff}<7200$ K with the distribution in $T_{\rm eff}$ set out in Figure 2.5 (b). The distribution of temperatures within the candidate list is weighted towards the hotter end of the stellar sample, with a significant peak just below 7000 K. There are two systems displaying approximately solar temperature ($T_{\rm eff}= 5780$ K) and one system with a temperature much lower than the solar: TIC 124280718 has an effective temperature of just 5249 K.

It may be difficult to obtain high precision radial velocity measurements for the hottest of our candidates, as they are likely to be rapidly rotating or have few good absorption lines for cross-correlation (Verschueren et al., 1999). However, we have seven candidates with effective temperatures <6500 K. These candidates should be most amendable to radial velocity confirmation.

Our search criteria was targeted at very short period planet candidates, as these systems have the highest amplitude phased photometric variations. Therefore the period range of our candidates is limited to 0.65 to 1.98 days. The distribution of periods within the candidate list is set out in Figure 2.5 (c). We see a slight peak in the periods at approximately P=1 day, and another peak just before the P=2 days cutoff. In addition to producing the largest amplitude phased photometric variation signals, these short period candidates will also give large amplitude of radial velocity signals, as the radial velocity semi-amplitude (K) scales with period as $K \propto P^{-\frac{1}{3}}$ (Lovis and Fischer, 2010).

The photometric amplitudes of our candidates are set out in Figure 2.5 (d). They range from 96 ppm to 528 ppm. There is a peak clearly visible around 200 ppm, which is likely a result of the stipulated lower bound of 200 ppm for signals detected in individual sectors, as set out in Section 2.3.3. When the 3-component model is applied to multiple sectors for each candidate, there are four systems presenting at amplitudes lower the 200 ppm.

The distribution of estimated planet radii for the candidate systems is set out in Figure 2.5 (e). As seen in the data, we expect many of these candidates to be inflated hot Jupiters with $R_p > 1.4R_J$ (Bodenheimer et al., 2001; Sestovic et al.,

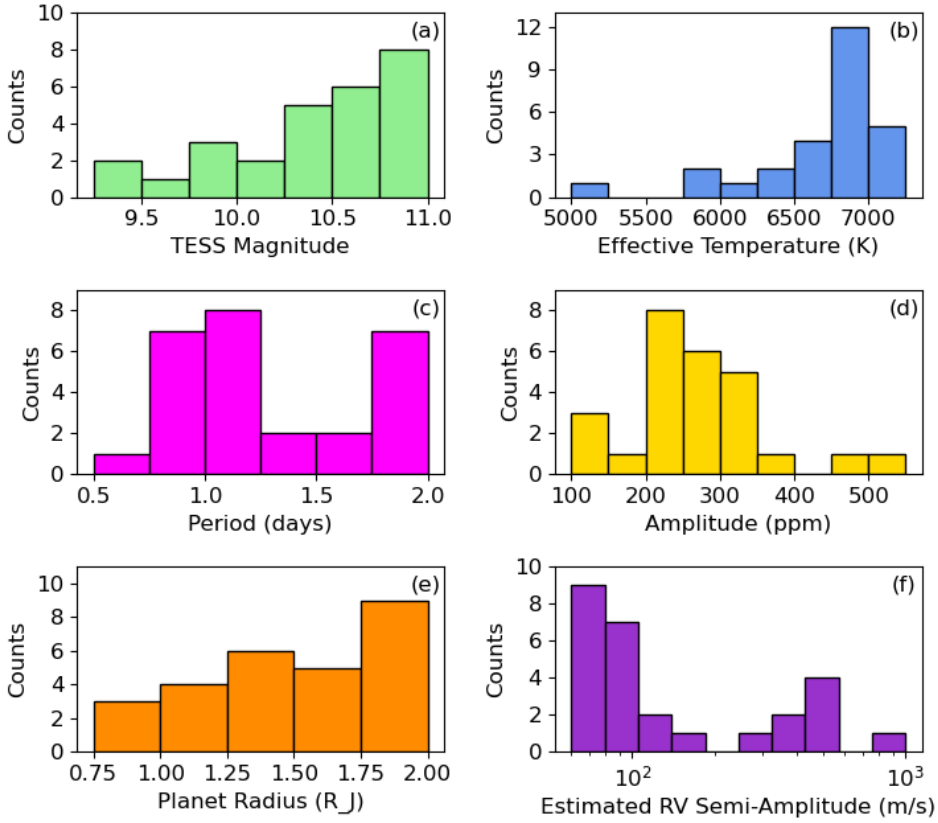

Figure 2.5: Histograms representing the distribution of various parameters within our phased photometric variation candidate list: (a) *TESS* magnitudes, (b) stellar effective temperatures, (c) orbital periods, (d) phased photometric variation amplitudes, (e) planet radii, (f) estimated radial velocity semi-amplitudes.

2018), as they orbit very close to their host stars.

The calculated radial velocity semi-amplitudes range from 61 to 997 $\mathrm{m\,s^{-1}}$. We present the distribution of these semi-amplitude in Figure 2.5 (f). We note that such radial velocity amplitudes are easily within reach of modern planet-hunting spectrographs such as HARPS, which has precision on the order of 1 $\mathrm{m\,s^{-1}}$(Mayor et al., 2003).

2.5.2 Comparison with Known Systems

In order to determine if the properties of our candidates are consistent with the systems known to show phased photometric variation, we compare our candidates to a set of selected confirmed transiting hot Jupiters with TESS detected phased photometric variation. These selected systems are set out in Table 2.1, and are primarily taken from the works of Wong et al. (2020) and Wong et al. (2021b). We expect our planets to closely match these known transiting planets as we designed our search to find the non-transiting analogues of these very hot Jupiters.

In Figure 2.6 (a) we plot the magnitude and phased photometric variation amplitude of our candidates in comparison to the known sample, demonstrating that these systems are similar in these properties. We also show the effective temperature of the candidate host stars and the known sample. The average of our candidate sample is approximately 100 K above the known sample.

In Figure 2.6 (b) we plot the estimated planet radius and period for each candidate system in comparison to the known sample, coloured by the stellar effective temperature. The strong upward trend in radius at longer periods is a direct result of the strong dependency on planetary radius for atmospheric modulation (see Equation 2.1). Atmospheric modulation is usually the most prominent phased photometric variation component and as such, larger radius planets are needed in order to produce detectable signals at longer periods.

2.5.3 Individual Candidates

A number of individual candidates are of special interest, and we outline them here.

- **TIC 124280718** has the lowest effective temperature in the candidate list with $T_{\mathrm{eff}} = 5249$ K. Furthermore, with an estimated planetary mass of 1.83 $M_J$and orbital period of 0.88 days, the system has one of the highest estimated radial velocity semi-amplitudes amongst the candidates: $K sin(i) = 417\,\mathrm{m\,s^{-1}}$. Combined, these two properties make TIC 124280718 an ideal candidate for confirmation via radial velocity measurements.

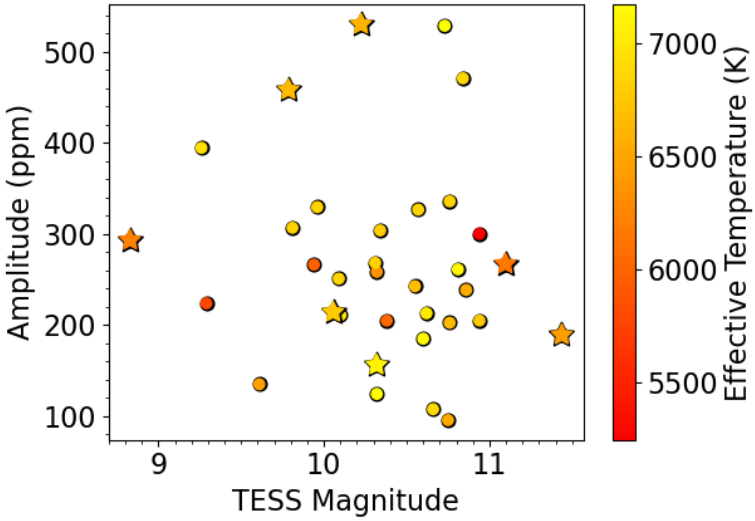

(a) The phased photometric variation signal amplitudes as a function of *TESS* magnitude for our candidates (circles) and a sample of stars with known planets giving detectable phased photometric variation in *TESS* (stars - see Table 2.1). The host star effective temperatures are shown via the colour bar, ranging from hot (yellow) to cool (red).

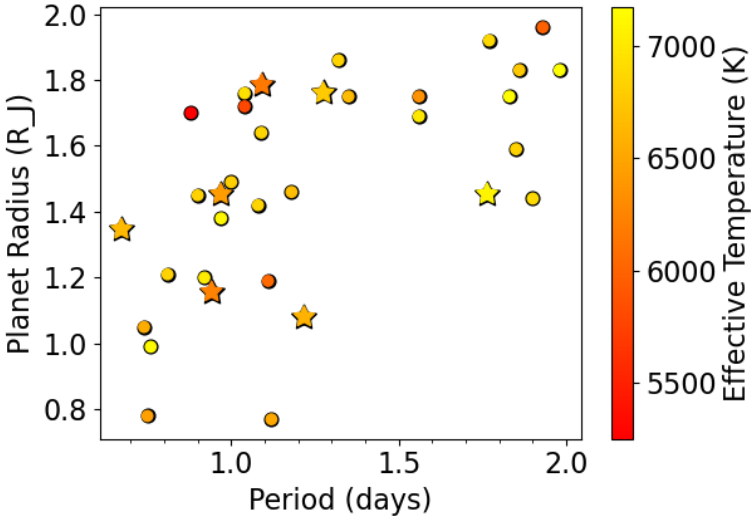

(b) The estimated planet radii as a function of period for our candidates (circles) and a sample of stars with known planets giving detectable phased photometric variation in *TESS* (stars - see Table 2.1). The host star effective temperatures are shown via the colour bar, ranging from hot (yellow) to cool (red).

Figure 2.6: Comparison of system parameters for known and candidate planets.

- **TIC 235055610** is a candidate with a signal detected in a total of 6 sectors - the highest number of detected sectors in the candidate list. The system has the highest planetary mass in the candidate list with a mass of $7.98\,\mathrm{M}_J$. As a result, TIC 124280718 has one of the highest tidal ellipsoidal distortion contributions with $A_{ellip} = 54.0\,\mathrm{ppm}$, and the highest estimated radial velocity semi-amplitude of $Ksin(i) = 997\,\mathrm{m\,s^{-1}}$.

- **TIC 362086194** is also a candidate with a signal detected in a total of 6 sectors. The system has the highest tidal ellipsoidal distortion contributions with $A_{ellip} = 64.3\,\mathrm{ppm}$. However, it has the lowest total amplitude across all sectors with a combined signal of just $A = 95.5\,\mathrm{ppm}$.

- **TIC 56126064, TIC 174001896** and **TIC 443857085** have high values for α_{atm}: 7.2, 7.2 and 10.8 respectively. These values have been adjusted outside of the guide range of known planets in order for the model to reasonably fit the data. These systems all have large planetary masses ($> 3\,\mathrm{M}_J$), high host star effective temperatures ($> 6832\,\mathrm{K}$), and orbital periods on the long end of our distribution ($> 1.77\,\mathrm{days}$).

- **TIC 56126064, TIC 454198279** and **TIC 200526405** all have non-single star markers from the *Gaia* data (Gaia Collaboration et al., 2016, 2018). These systems are flagged with a value of 2, indicating that they may be photometric binary systems.

2.6 Discussion

2.6.1 Radial Velocity Follow-up

The 27 phased photometric variation candidates presented in this work are all potentially non-transiting, very short period hot Jupiter systems. The best way to confirm these exoplanets is to search for the characteristic planet-induced radial velocity variation on the host star via spectroscopic monitoring. Such monitoring was able to confirm similar candidates found in the Kepler mission (Lillo-Box et al., 2021). Our candidates will be easier to follow-up spectroscopically than the Kepler candidates as the host stars are much brighter. However as noted in Chapter 2.5.1, some of the candidate host stars are hot and may cause difficulties for precise radial velocity measurements.

2.6.2 Photometric Follow-up

In addition to confirming the candidates via radial velocity monitoring, it would also be possible to confirm the photometric signal. For this we would need to reach a precision of at least 100 ppm per 30 mins over the duration of the orbital period. This would be a challenge for most ground-based telescopes, but would be in reach of ESA's CHaracterising ExOPlanets Satellite (CHEOPS; Benz et al., 2021). *CHEOPS* is a 30 cm space-based telescope tasked with characterising known exoplanets including the determination of planet radii, masses and compositions. *CHEOPS* has already measured phase curves of hot Jupiters, including WASP-189 b (Lendl et al., 2020; Deline et al., 2022), HD 209458 b (Brandeker et al., 2022) and MASCARA-1 b (Hooton et al., 2022). Photometry from *CHEOPS* could help characterise and disentangle the three components of the phased photometric variation. All of our candidates are within the magnitude limit for *CHEOPS*, although some of the candidates may not be in suitable positions in the sky for good observations via *CHEOPS*.

2.6.3 Future TESS Phased Photometric Variation Searches

Starting in September 2022, the fifth year of the TESS mission begins, with observations comprising of Sectors 56-69. During Year 5, TESS will observe sections of sky in both the northern and southern hemispheres (Huang et al., 2018). The spacecraft's return to the southern hemisphere will provide additional data to many of the systems considered in this project, including 16 of the 27 systems in the candidate list.

The future of the *TESS* mission will provide an opportunity to continue searching for non-transiting planets. In this project we have focused on *TESS* data from the south ecliptic hemisphere, which comprises of Year 1 and Year 3 observations. A similar search could also be conducted in the northern ecliptic hemisphere and the ecliptic plane.

The northern ecliptic hemisphere is made up of Year 2 and Year 4 data. Compared to the South, the total area of observation in the North is less complete: the spacecraft pointing was adjusted to avoid excessive contamination by stray moonlight.

In the fourth year of the mission, the *TESS* field-of-view was rotated to cover a portion of the ecliptic region. These observations included targets from Camera 1 of both the first and second year of the mission, as well as covering a previously unobserved region. Observations of the ecliptic region will be repeated in the sixth

year of the mission.

Throughout the duration of mission, TESS will observe most of the sky, with a large portion of targets appearing in at least 2 sectors of observations. The nature of *TESS*'s repeat observations and near-complete sky coverage results in a large amount of data continually becoming available which is suitable for future phased photometric variation searches.

2.6.4 PLATO

The PLAnetary Transits and Oscillations of stars mission (PLATO; Rauer et al., 2014) is a mid-class space mission due to launch in 2026 by the European Space Agency (ESA). PLATO will have a photometric precision of approximately 50 ppm per hour for stars with V<11 and approximately 150 ppm per hour for a larger set of stars with V<13 (Rauer et al., 2014; Montalto et al., 2021). Unlike *TESS*, *PLATO* will employ long duration monitoring campaigns that will involve a year or more of continuous photometry for a single field (Nascimbeni et al., 2022). This will be ideal for picking up the subtle phased photometric variation signals from non-transiting exoplanet systems. Given the majority of transiting giant planets around bright stars will already have been discovered over the last two decades, the primary method of discovery for giant planets in the *PLATO* mission may well be via phased photometric variation.

2.7 Conclusion

The prospect of using phased photometric variations for the detection of non-transiting planets is relatively unexplored compared to other planet detection methods, despite being successfully applied to systems in the Kepler data set (Millholland and Laughlin, 2017; Lillo-Box et al., 2021).

In this paper, we have presented the first discovery search for non-transiting planets using optical phase curves from the *TESS* mission. The method exploits the temporally consistent nature of planetary phase curves in comparison to other modes of light-curve variability, thus allowing the distinction of planetary signals.

We developed a pipeline to identify phased photometric variations in *TESS* light-curves from Years 1 and 3 of the mission. In total, we identify 27 non-transiting planet candidates, each with good prospects for radial velocity confirmation. Combined with phase curve detections, radial velocity measurements will not only allow the confirmation of these planet candidates, but will also deepen our knowledge of each system's parameters and dynamics (Lillo-Box et al., 2021). We are con-

fident that the methods applied in this paper can be applied to data from future space-based missions such as *PLATO*.

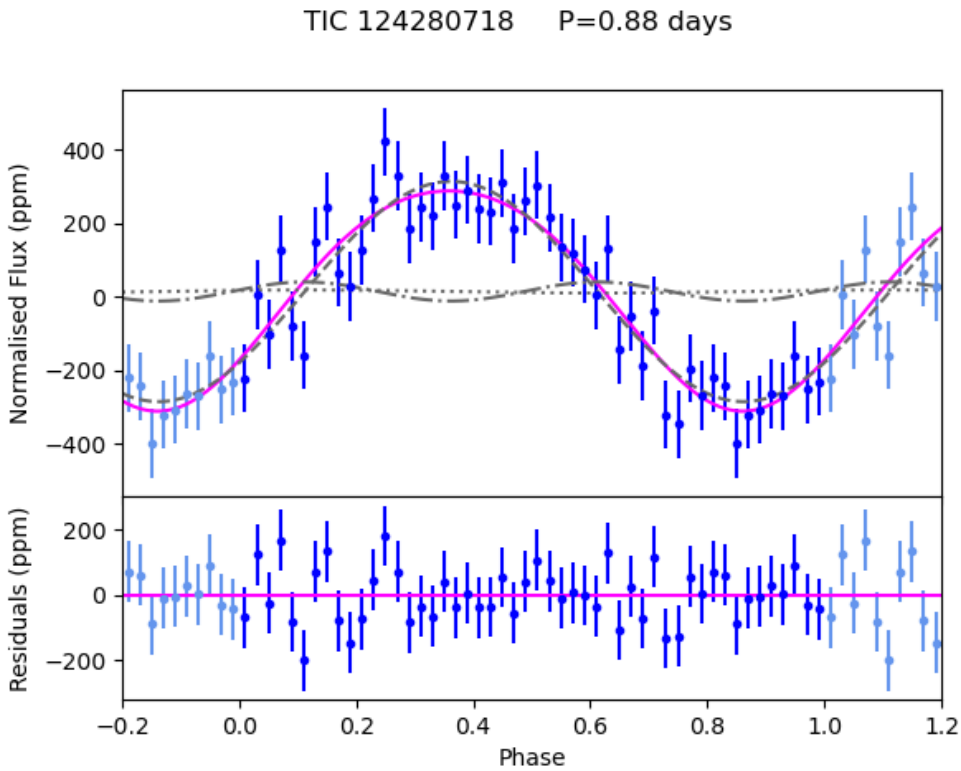

Figure 2.7: Individual phase curve components with combined three-component model (top) and associated residuals (bottom) for TIC 124280718. The data is binned to 50 points (shown in dark blue), with recurring data points shown in light blue. The three phase curve components are: atmospheric modulation (grey dashed line), tidal ellipsoidal distortion (grey dash-dot line), and Doppler beaming (grey dotted line). The combined model is shown with a solid pink line. The residuals shown in the bottom panel are relative to the combined three-component model.

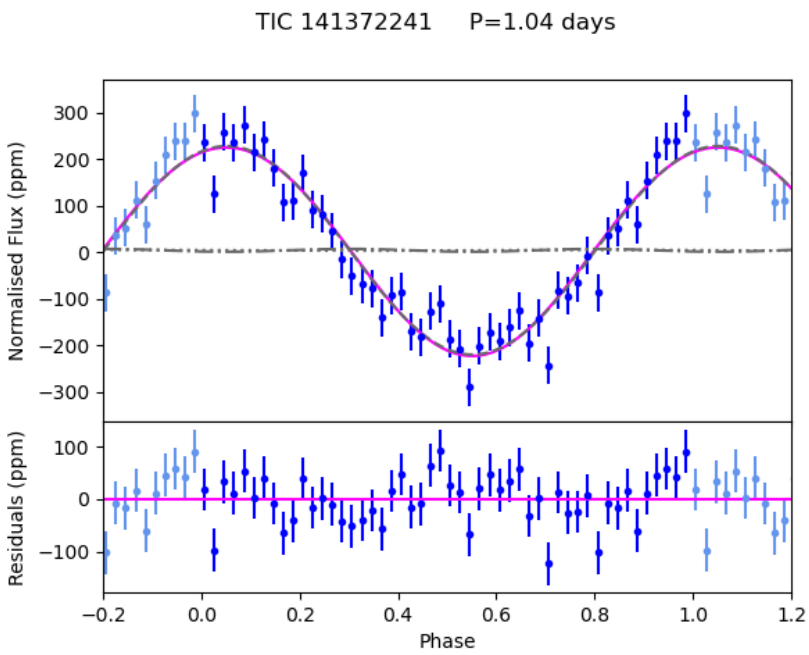

Figure 2.8: Individual phase curve components with combined three-component model (top) and associated residuals (bottom) for TIC 141372241. The lines shown in this figure are the same as for Figure 2.7.

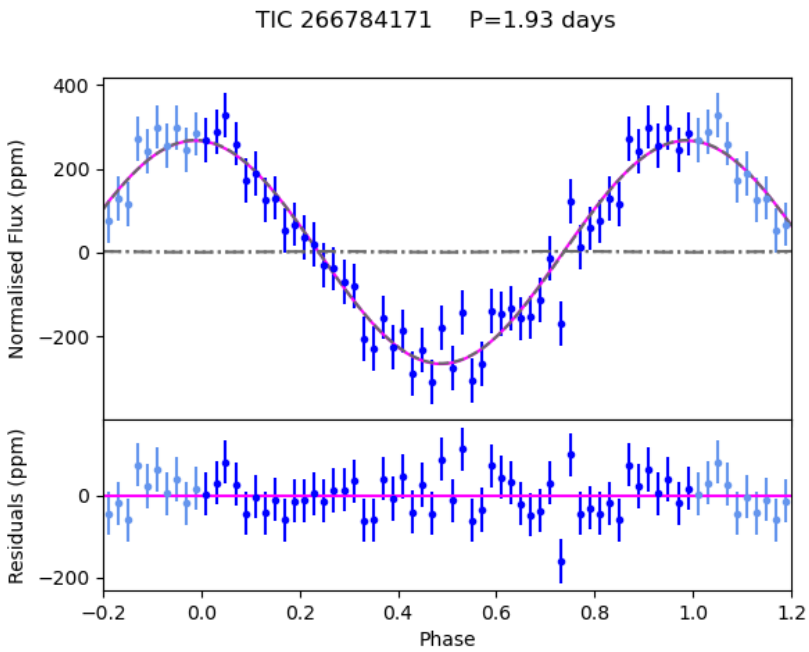

Figure 2.9: Individual phase curve components with combined three-component model (top) and associated residuals (bottom) for TIC 266784171. The lines shown in this figure are the same as for Figure 2.7.

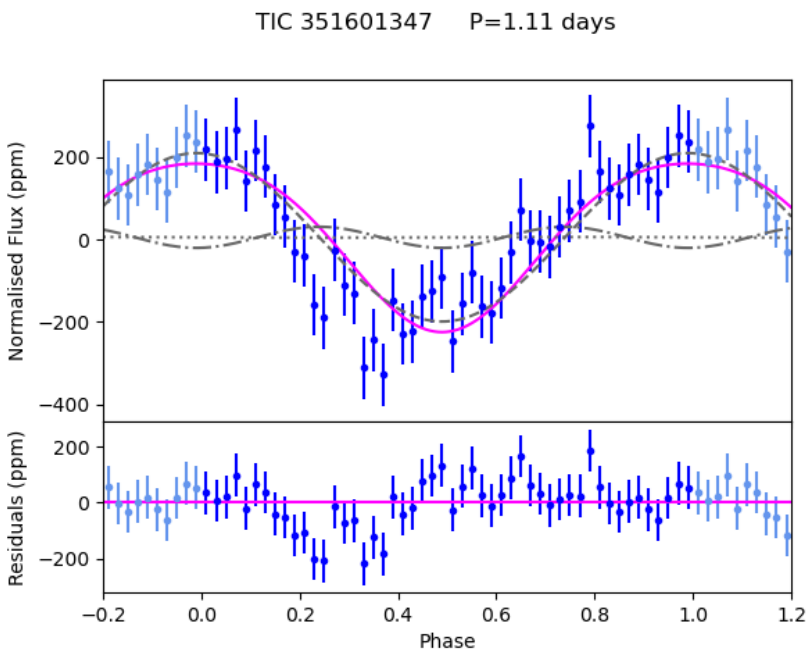

Figure 2.10: Individual phase curve components with combined three-component model (top) and associated residuals (bottom) for TIC 351601347. The lines shown in this figure are the same as for Figure 2.7.

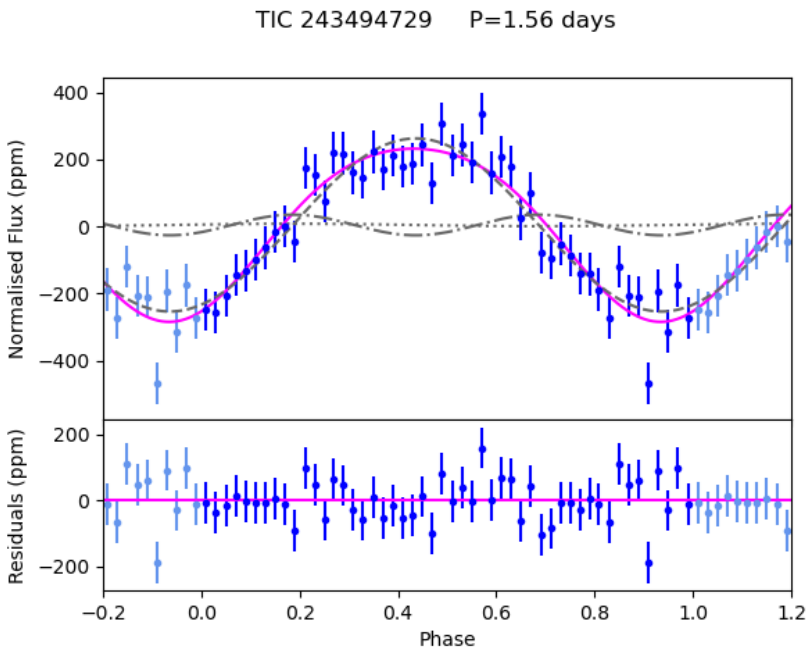

Figure 2.11: Individual phase curve components with combined three-component model (top) and associated residuals (bottom) for TIC 243494729. The lines shown in this figure are the same as for Figure 2.7.

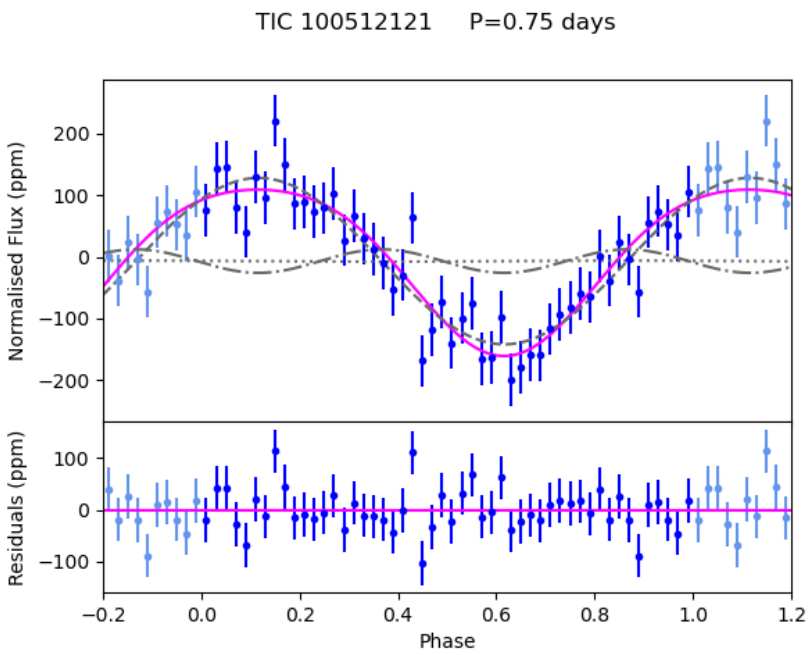

Figure 2.12: Individual phase curve components with combined three-component model (top) and associated residuals (bottom) for TIC 100512121. The lines shown in this figure are the same as for Figure 2.7.

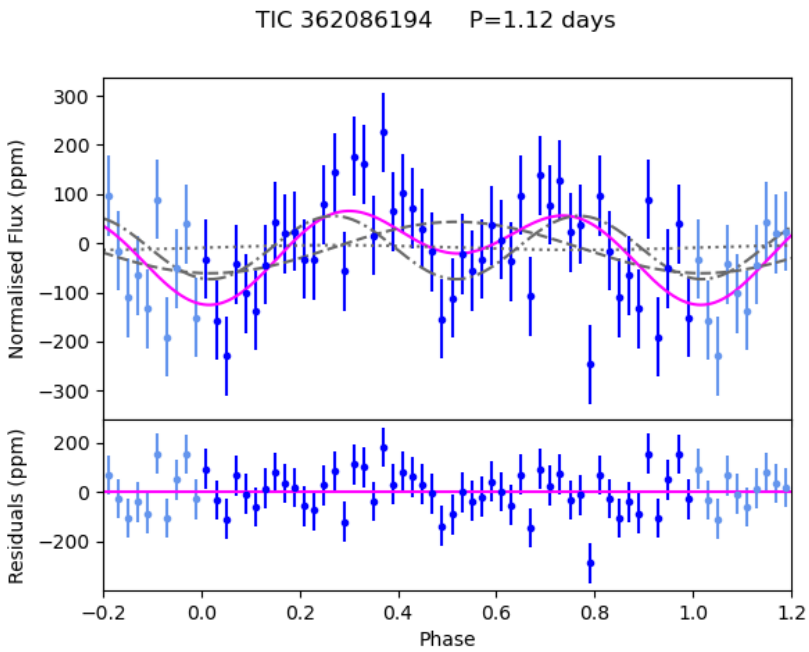

Figure 2.13: Individual phase curve components with combined three-component model (top) and associated residuals (bottom) for TIC 362086194. The lines shown in this figure are the same as for Figure 2.7.

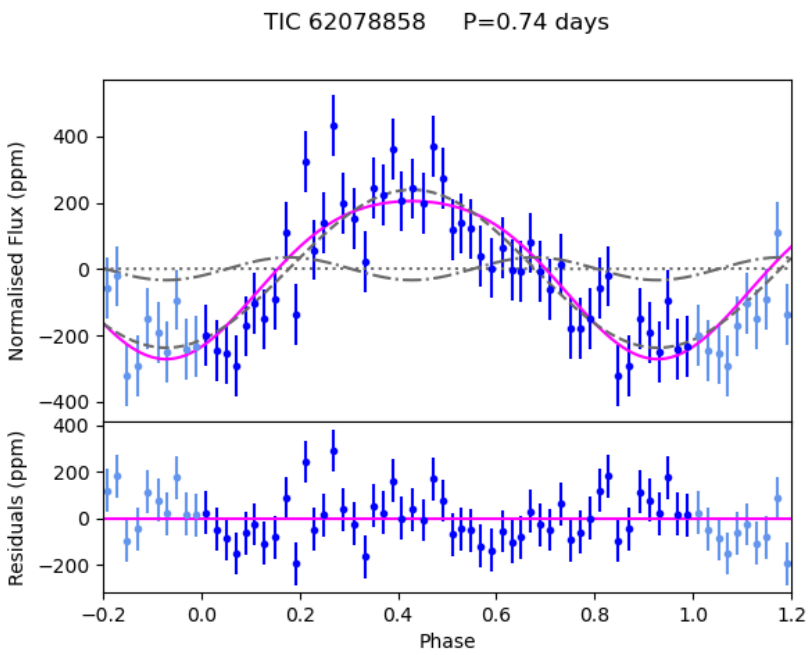

Figure 2.14: Individual phase curve components with combined three-component model (top) and associated residuals (bottom) for TIC 62078858. The lines shown in this figure are the same as for Figure 2.7.

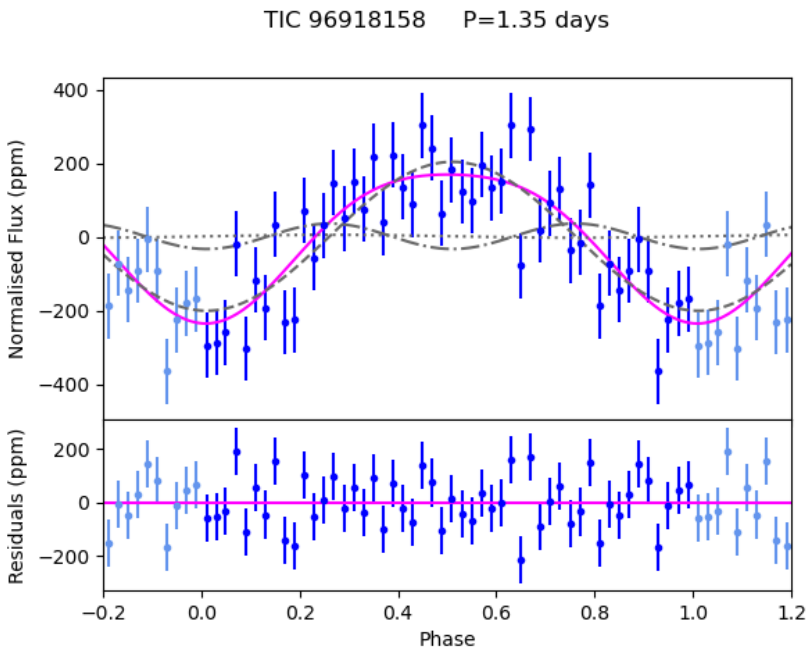

Figure 2.15: Individual phase curve components with combined three-component model (top) and associated residuals (bottom) for TIC 96918158. The lines shown in this figure are the same as for Figure 2.7.

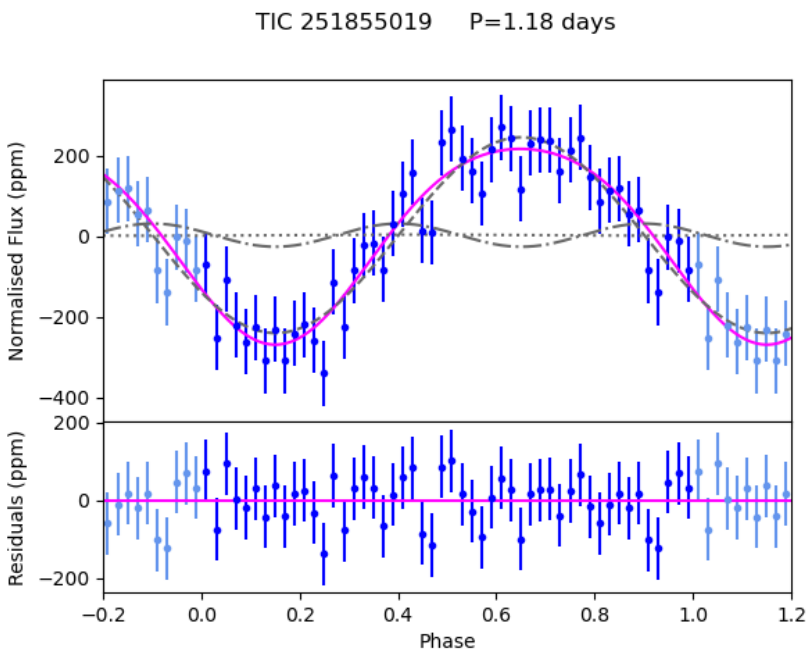

Figure 2.16: Individual phase curve components with combined three-component model (top) and associated residuals (bottom) for TIC 251855019. The lines shown in this figure are the same as for Figure 2.7.

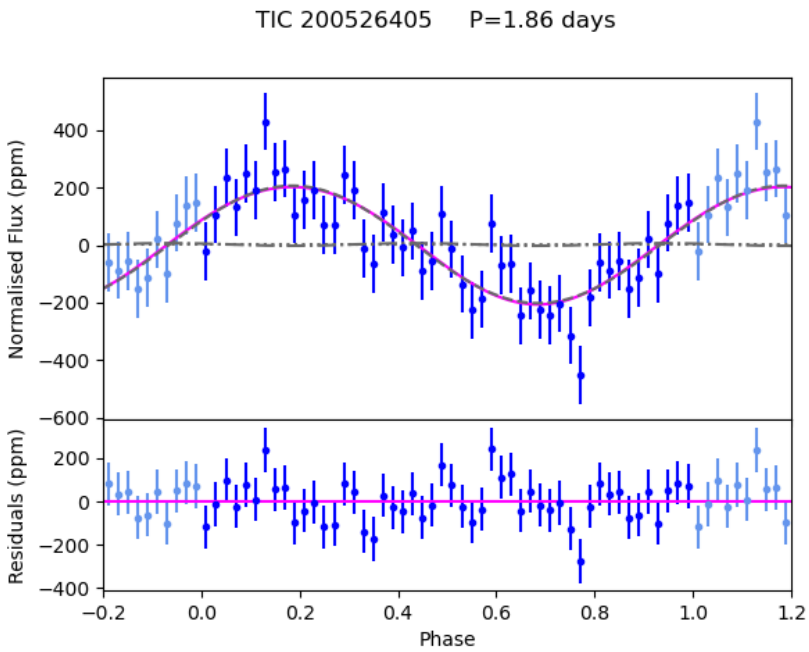

Figure 2.17: Individual phase curve components with combined three-component model (top) and associated residuals (bottom) for TIC 200526405. The lines shown in this figure are the same as for Figure 2.7.

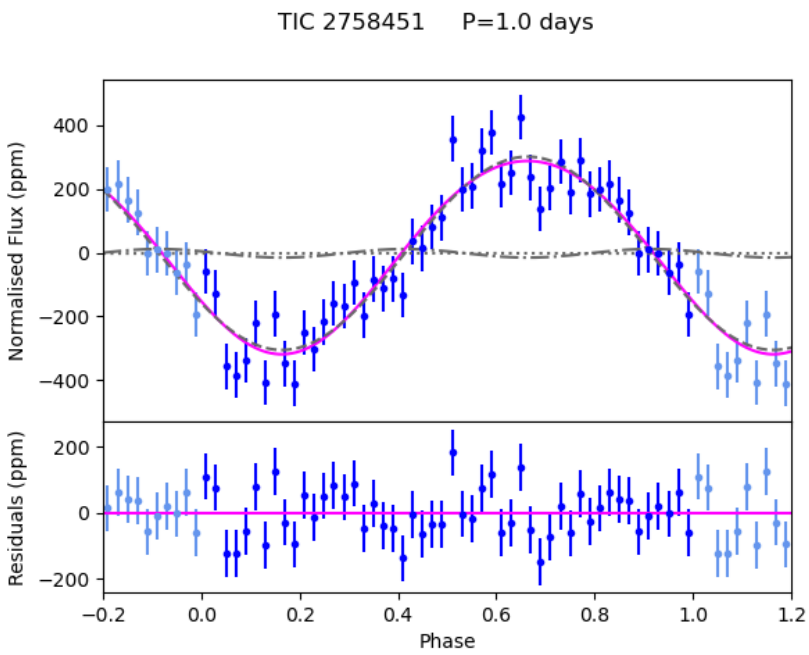

Figure 2.18: Individual phase curve components with combined three-component model (top) and associated residuals (bottom) for TIC 2758451. The lines shown in this figure are the same as for Figure 2.7.

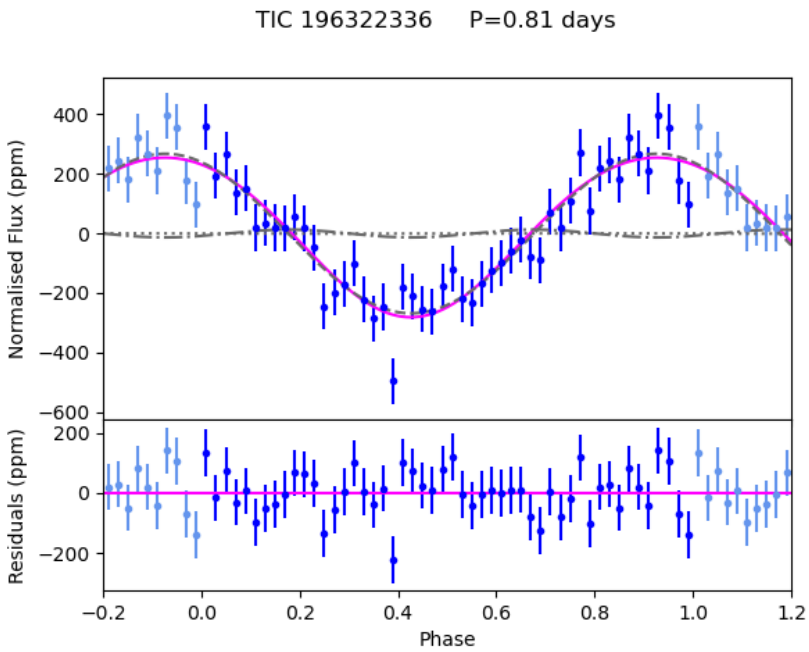

Figure 2.19: Individual phase curve components with combined three-component model (top) and associated residuals (bottom) for TIC 196322336. The lines shown in this figure are the same as for Figure 2.7.

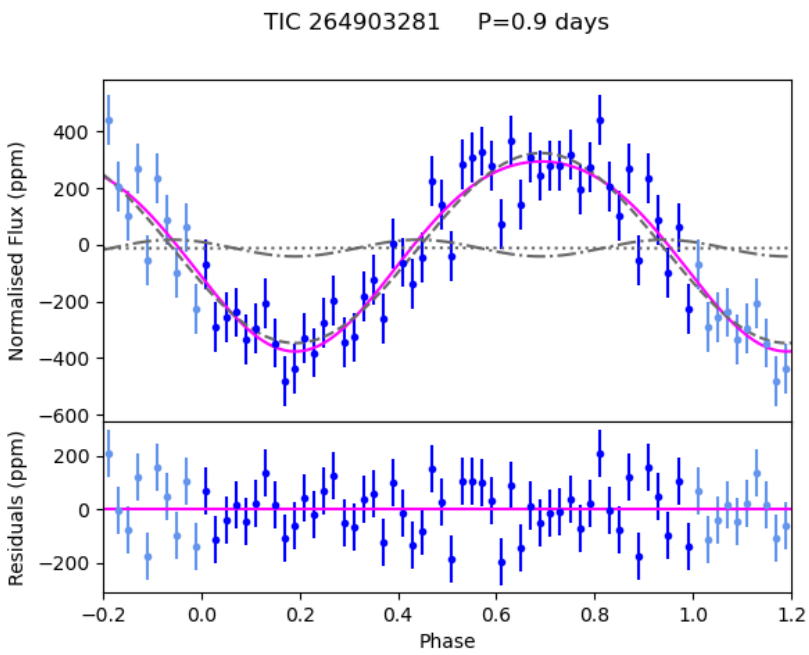

Figure 2.20: Individual phase curve components with combined three-component model (top) and associated residuals (bottom) for TIC 264903281. The lines shown in this figure are the same as for Figure 2.7.

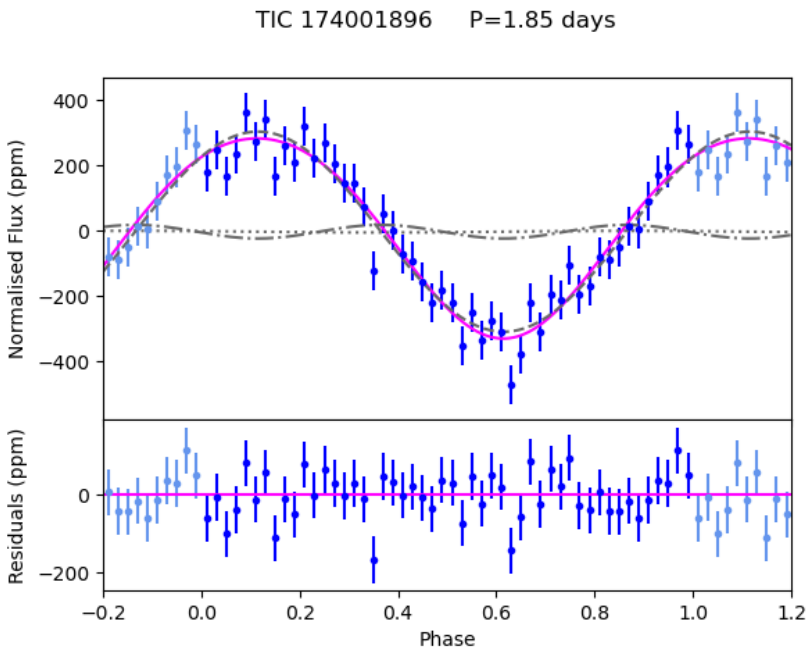

Figure 2.21: Individual phase curve components with combined three-component model (top) and associated residuals (bottom) for TIC 174001896. The lines shown in this figure are the same as for Figure 2.7.

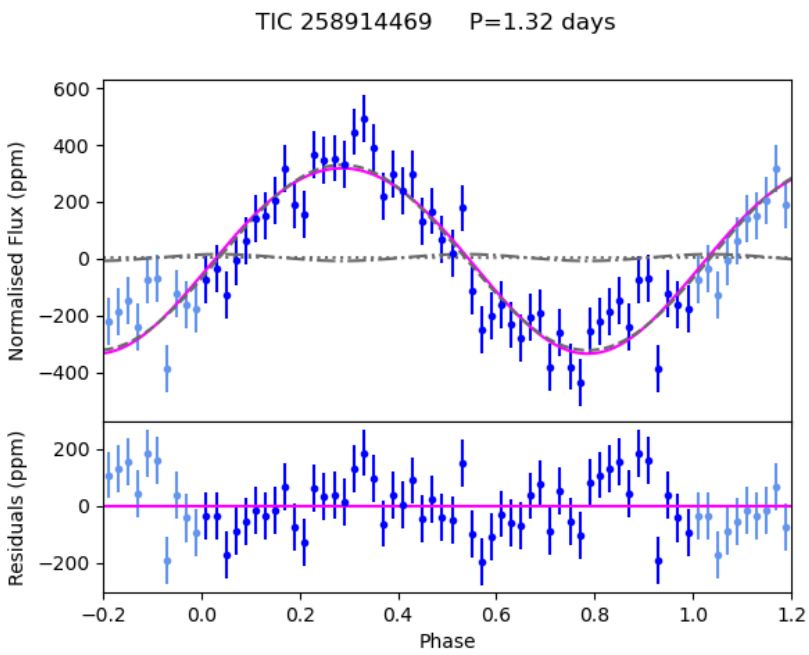

Figure 2.22: Individual phase curve components with combined three-component model (top) and associated residuals (bottom) for TIC 258914469. The lines shown in this figure are the same as for Figure 2.7.

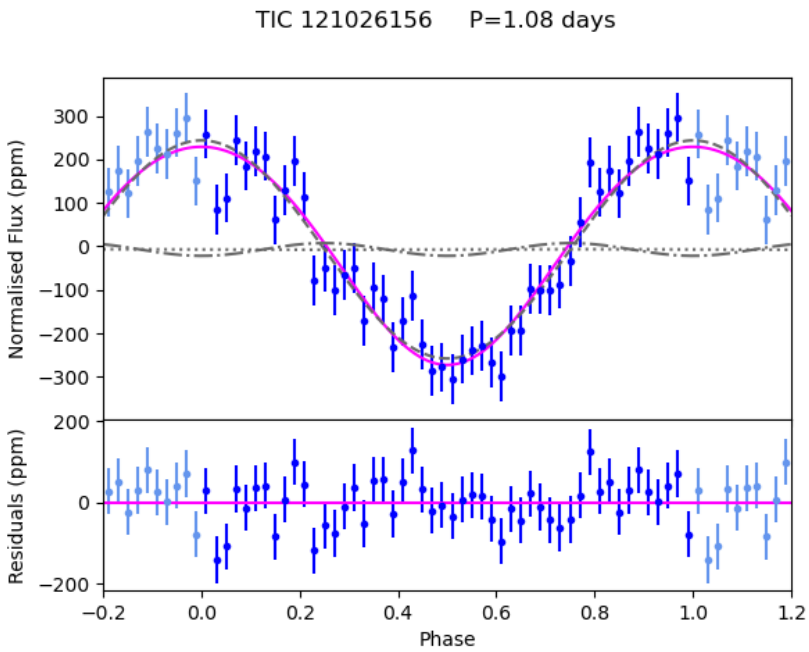

Figure 2.23: Individual phase curve components with combined three-component model (top) and associated residuals (bottom) for TIC 121026156. The lines shown in this figure are the same as for Figure 2.7.

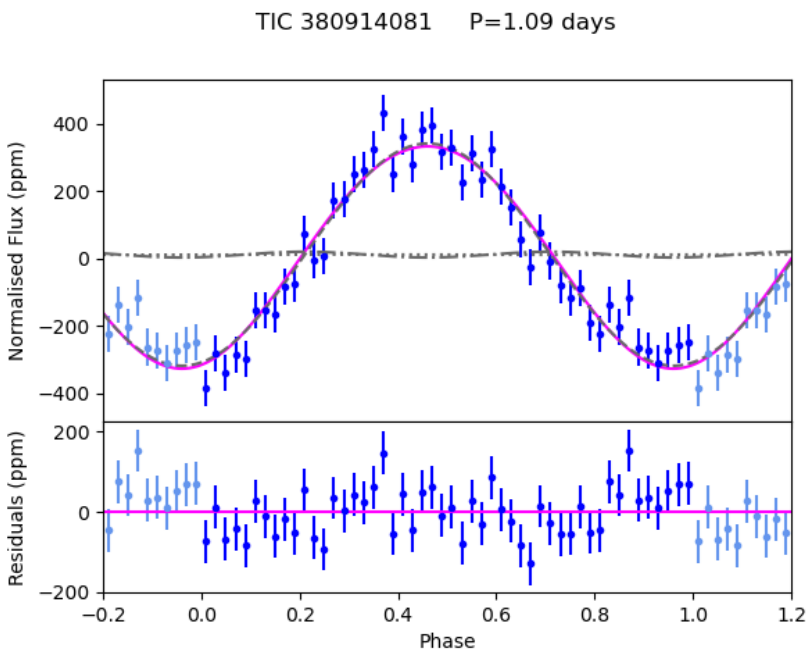

Figure 2.24: Individual phase curve components with combined three-component model (top) and associated residuals (bottom) for TIC 380914081. The lines shown in this figure are the same as for Figure 2.7.

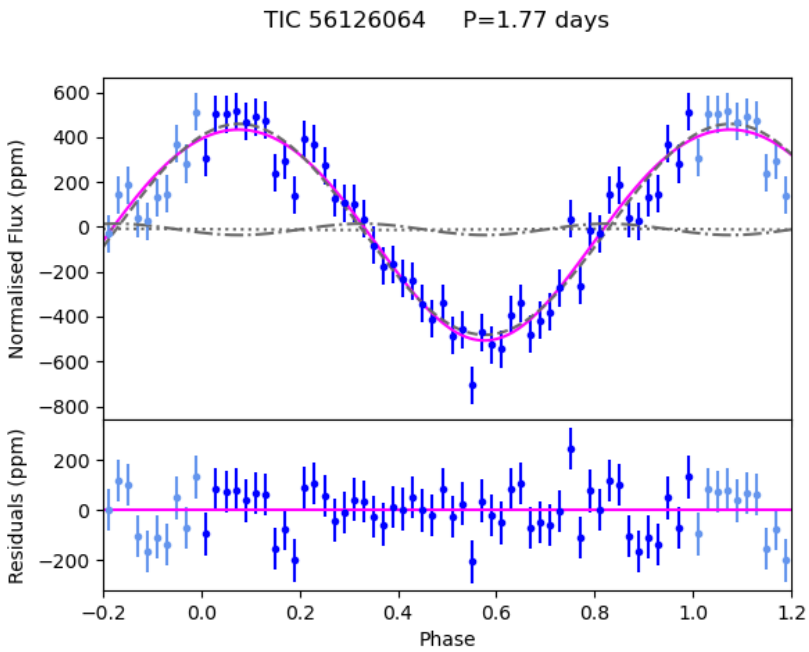

Figure 2.25: Individual phase curve components with combined three-component model (top) and associated residuals (bottom) for TIC 56126064. The lines shown in this figure are the same as for Figure 2.7.

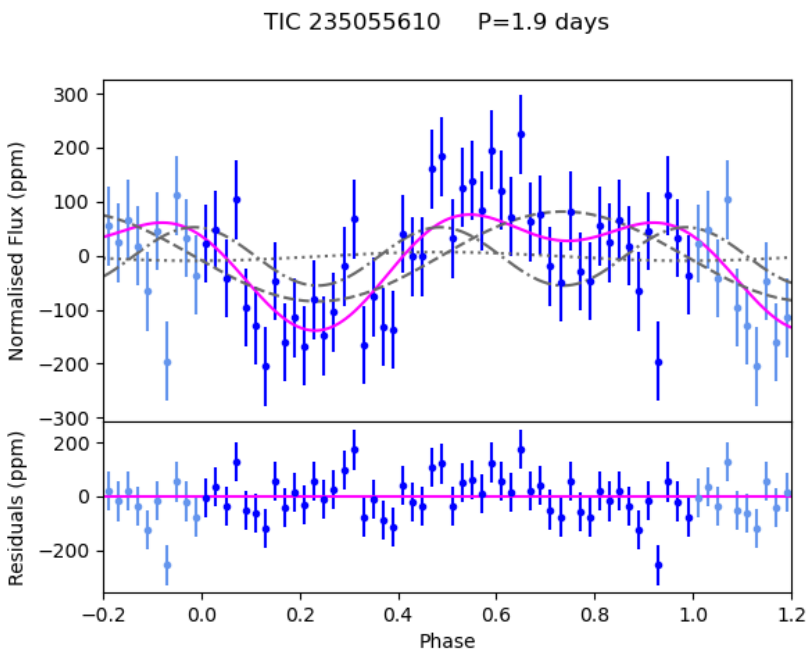

Figure 2.26: Individual phase curve components with combined three-component model (top) and associated residuals (bottom) for TIC 235055610. The lines shown in this figure are the same as for Figure 2.7.

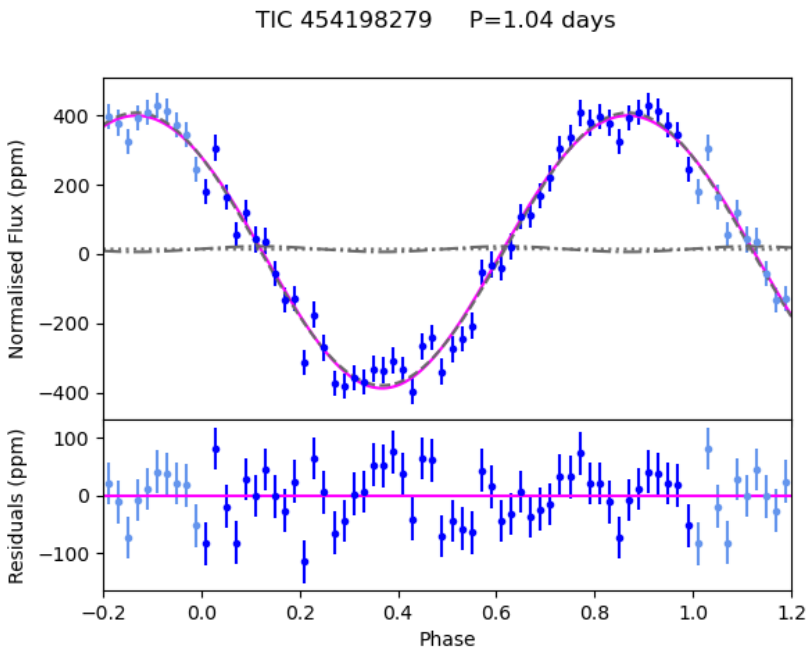

Figure 2.27: Individual phase curve components with combined three-component model (top) and associated residuals (bottom) for TIC 454198279. The lines shown in this figure are the same as for Figure 2.7.

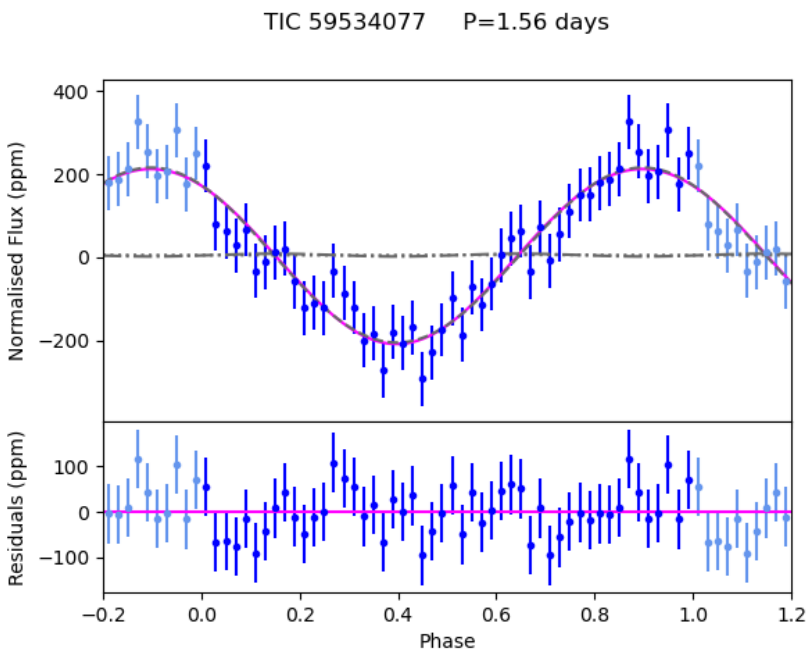

Figure 2.28: Individual phase curve components with combined three-component model (top) and associated residuals (bottom) for TIC 59534077. The lines shown in this figure are the same as for Figure 2.7.

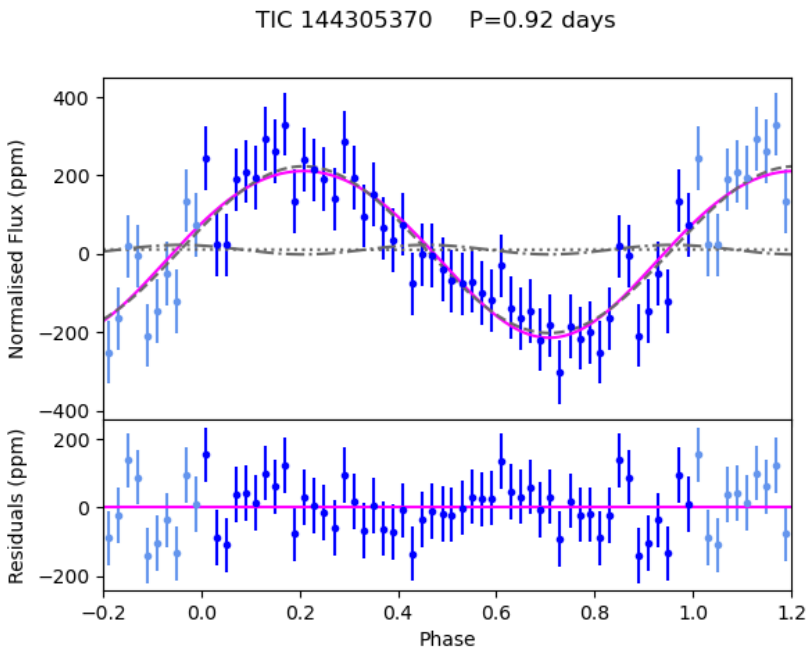

Figure 2.29: Individual phase curve components with combined three-component model (top) and associated residuals (bottom) for TIC 144305370. The lines shown in this figure are the same as for Figure 2.7.

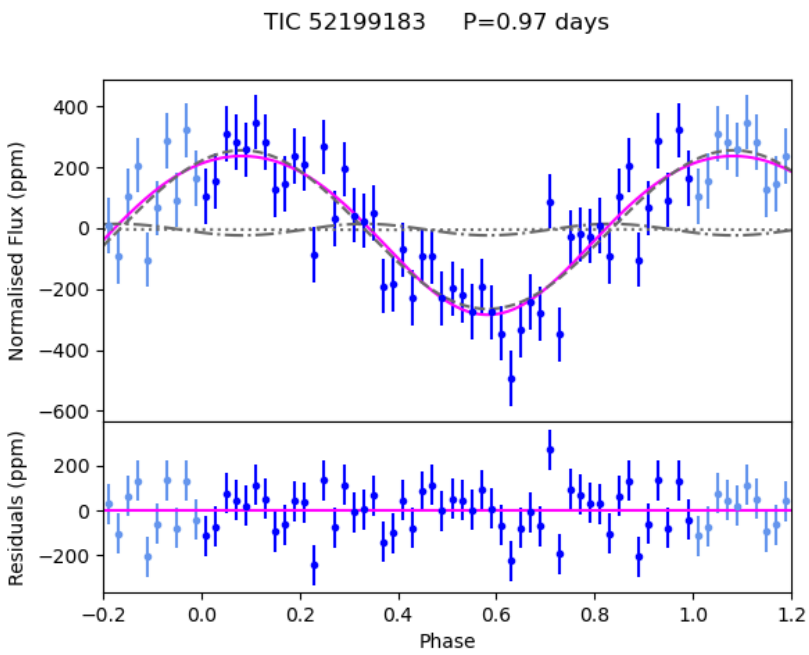

Figure 2.30: Individual phase curve components with combined three-component model (top) and associated residuals (bottom) for TIC 52199183. The lines shown in this figure are the same as for Figure 2.7.

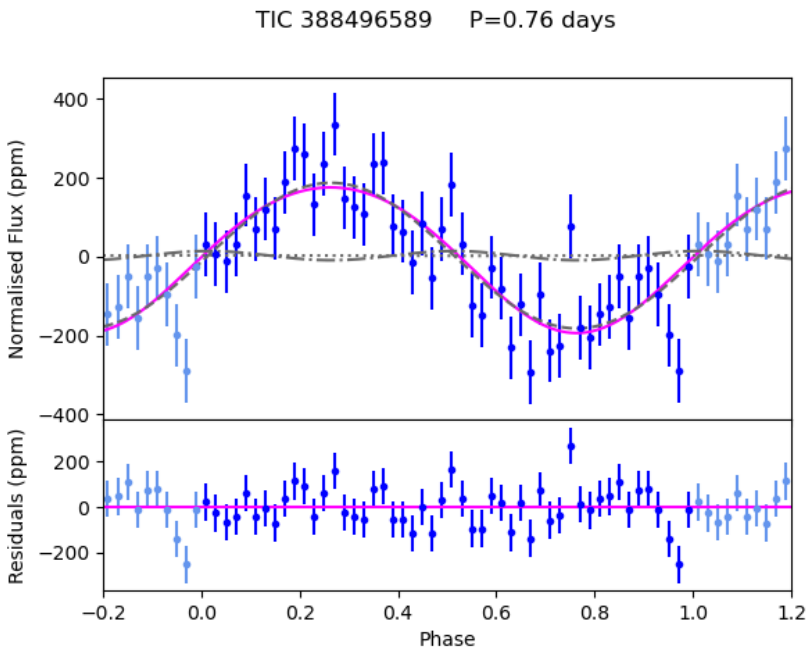

Figure 2.31: Individual phase curve components with combined three-component model (top) and associated residuals (bottom) for TIC 388496589. The lines shown in this figure are the same as for Figure 2.7.

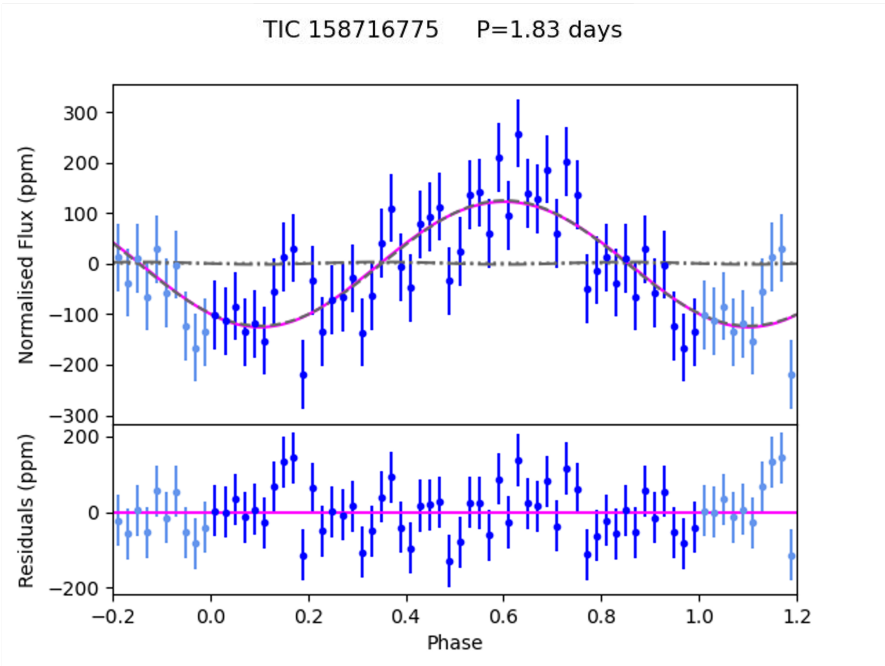

Figure 2.32: Individual phase curve components with combined three-component model (top) and associated residuals (bottom) for TIC 158716775. The lines shown in this figure are the same as for Figure 2.7.

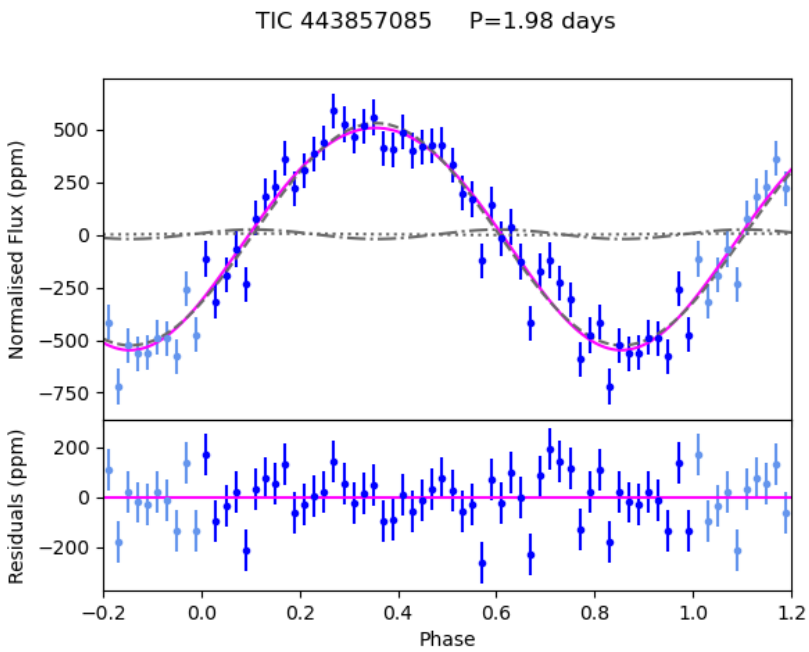

Figure 2.33: Individual phase curve components with combined three-component model (top) and associated residuals (bottom) for TIC 443857085. The lines shown in this figure are the same as for Figure 2.7.

Chapter 3

Conclusion

In this thesis, we present a search for non-transiting exoplanets with phased photometric variations from *TESS* photometry. We use a sample of 140,000 stars with full-frame light-curves from Years 1 and 3 of the *TESS* mission. Applying a modified Lomb-Scargle algorithm, we search the light-curves for significant periodic signals between 0.5 and 2.0 days. We vet the candidates based on the properties of known transiting exoplanets with phased photometric variations, searching for low-amplitude, near-sinusoidal, temporally consistent signals with light-curves indicative of the existence of exoplanets. We fit the phased photometric variation signal with a three-component model comprised of atmospheric modulation, tidal ellipsoidal distortion, and Doppler beaming components. We find 27 systems that may host short-period, massive planets.

Each of the 27 candidate systems has a cool, bright, isolated host star with $Tmag < 11$, and $T_{\rm eff}$ ranging between 5249 and 7171 K. The systems have great potential for radial velocity follow up measurements to confirm them as planets and obtain more precise values for planetary masses.

The work in this thesis demonstrates the ability of *TESS* to discover non-transiting planets with phased photometric variations, and, if confirmed, these candidates could open a new door to non-transiting exoplanet detection with current and upcoming data from the *TESS* and *PLATO* missions.

3.1 Method Improvements

Despite the obvious success outlined in Section 2.5, there are some areas where minor improvements could build on the research methods presented in this thesis.

Primarily, in Section 2.3.4, we outline a method of candidate selection based

on consistent signals. In particular, we accept only candidate systems with coherent phase across multiple sectors. This phase matching process is intended to ensure all candidates are temporally consistent (a key property of planetary signals). However, we allow a margin of ± 0.2 units of phase which equates to 40% of the total phase window. The most common separation between periods of observation is 27 sectors, which equates to approximately 700 days. For our candidates with a period range of 0.74 to 1.98 days, the error in the period measurement would have to be on the order of 1×10^{-4} or lower, in order to meet this restriction. Currently, the sensitivity of period measurements from the Lomb-Scargle process applied in Section 2.3.1 is not to this scale. In addition to modifying the LS algorithm, one method to improve this selection process is to introduce a new phase matching restriction that is dependent on both the period of the system and the number of sectors that have elapsed between observations.

Furthermore, we note that the simple threshold cuts applied Section 2.3.4 are relatively relaxed at short periods (close to 0.5 days) and stringent at longer periods (close to 2 days). An alternative, fractional approach to these period and amplitude cuts may be more suitable.

Changes to this selection process will likely result in a greater number of candidates passing on to the visual inspection phase where each candidate is manually assessed (see Section 2.4). Currently, this stage is time-consuming and unsuitable for larger numbers of candidate systems. As such, in this thesis we only progress the most promising candidates. In order to detect a larger number of non-transiting systems, without manually assessing the light-curve, aperture and model fit for each, this process could be automated in two ways: firstly, we could apply a machine learning approach, as used in Millholland and Laughlin (2017), to assess the shape of each phase curve based on the properties of known exoplanet phase curves. Secondly, we could apply an automated 'running window' process to evaluate the consistency of the phase curve signal across multiple sectors. The running window would evaluate the amplitude of the light-curve averaged across a set time window and disregard systems where the amplitude is inconsistent with time.

The changes suggested in this section could make a significant improvement to the method presented, however they fall outside the scope of this project.

3.2 Future Work

3.2.1 Candidate Confirmation

Lillo-Box et al. (2021) obtained radial velocity measurements for a sample of 10 tar-

gets from a phase curve search with *Kepler* data (Millholland and Laughlin, 2017). They successfully confirmed three non-transiting exoplanets and found supporting evidence for the existence of exoplanets in a further three systems, thus demonstrating the ability of radial velocity measurements to confirm non-transiting exoplanets.

The 27 non-transiting exoplanet candidates presented in this work are all amenable to radial velocity confirmation as demonstrated by the estimated semi-amplitude values in Table 2.2. Furthermore, these systems all host cool, bright, small stars perfect for spectroscopic monitoring of radial velocity variations. These systems will be observable with ground-based radial velocity facilities such as *HARPS* (Mayor et al., 2003) and *CORALIE* (Queloz et al., 2001) due their position in the southern ecliptic hemisphere and large amplitude signals. We have applied for 5 nights of observations to monitor our candidates on *HARPS* via the ESO P111 call. The outcome of this proposal should be known in late 2022.

3.2.2 Atmospheric Observations

Giant exoplanets, such as the candidates presented in this thesis, are ideal targets for follow-up atmospheric studies. Using infrared observations, the thermal profile of an exoplanet orbiting a bright star can be mapped (Knutson et al., 2009). Since our candidates are in ultra-short orbits around bright stars, they are amenable to detailed studies of their atmospheric phase curves with high-precision infrared instruments such as those available with the recently launched *JWST* (Gardner et al., 2006; Venot et al., 2020).

Furthermore, with very high precision optical photometry, such as *CHEOPS* (Benz et al., 2021), the reflected light from the exoplanet can be studied and the albedo measured (Deline et al., 2022).

This combination of thermal emission and optical reflection over the full phase of the orbit will help us understand the composition, structure, and variability of exoplanet atmospheres.

3.2.3 Future Missions

Looking to the future, a major upcoming mission for exoplanet discovery is the PLAnetary Transits and Oscillations of stars mission (*PLATO*; Rauer et al., 2014) which will survey the sky in search of potentially habitable planets around main-sequence stars. *PLATO* will have longer baseline observations and a higher photometric precision than *TESS*, lending it the ability to detect phased photometric variation signals with lower amplitudes. In this way, *PLATO* will have the capabil-

ity to extend the range of the method presented in this thesis, potentially detecting planets will smaller radii and at longer orbital periods.

To date, there have been several successful space missions dedicated to detecting transiting exoplanets including *CoRoT* (Auvergne et al., 2009), *Kepler* (Borucki et al., 2010), *K2* (Howell et al., 2014), and *TESS* (Ricker et al., 2015). As such, thousands of massive transiting exoplanets have been discovered and these discoveries are beginning to slow (see Figure 1.5); the majority of giant transiting exoplanets around bright stars have already been detected but there is still an entire population of giant non-transiting exoplanets yet to be explored. With the implementation of the improvements outlined in Chapter 3.1, the primary method of discovery for giant planets in the *PLATO* mission may well be via phased photometric variations.

Bibliography

Airy G.B., 1847. *MNRAS*, 16:385.

Akeson R.L. et al., 2013. PASP, 125(930):989.

Auvergne M. et al., 2009. A&A, 506(1):411–424.

Bakos G. et al., 2004. PASP, 116(817):266–277.

Bakos G.Á. et al., 2013. PASP, 125(924):154.

Beatty T.G. and Gaudi B.S., 2015. PASP, 127(958):1240.

Beleznay M. and Kunimoto M., 2022. MNRAS, 516(1):75–83.

Benz W. et al., 2021. *Experimental Astronomy*, 51(1):109–151.

Bodenheimer P., Lin D.N.C., and Mardling R.A., 2001. ApJ, 548(1):466–472.

Borucki W.J. et al., 2010. *Science*, 327(5968):977.

Brandeker A. et al., 2022. A&A, 659:L4.

Bruno G., 1584. On the infinite universe and worlds (1584).

Charbonneau D. et al., 2000. ApJ, 529(1):L45–L48.

Claret A. and Bloemen S., 2011. A&A, 529:A75.

Deline A. et al., 2022. A&A, 659:A74.

Delrez L. et al., 2016. MNRAS, 458(4):4025–4043.

Faigler S., 2016. *arXiv e-prints*, arXiv:1612.08846.

Faigler S. and Mazeh T., 2011. MNRAS, 415(4):3921–3928.

Faigler S. and Mazeh T., 2015. ApJ, 800(1):73.

Faigler S. et al., 2013. ApJ, 771(1):26.

Gaia Collaboration et al., 2016. A&A, 595:A1.

Gaia Collaboration et al., 2018. A&A, 616:A1.

Gardner J.P. et al., 2006. Space Sci. Rev., 123(4):485–606.

Gingerich O., 1985. *Journal for the History of Astronomy*, 16:37.

Hebb L. et al., 2009. ApJ, 693(2):1920–1928.

Hellier C. et al., 2009a. Nature, 460(7259):1098–1100.

Hellier C. et al., 2009b. Nature, 460(7259):1098–1100.

Hellier C. et al., 2014. MNRAS, 440(3):1982–1992.

Henry G.W. et al., 2000. ApJ, 529(1):L41–L44.

Herschel W. and Watson D., 1781. *Philosophical Transactions of the Royal Society of London Series I*, 71:492–501.

Hooton M.J. et al., 2022. A&A, 658:A75.

Howell S.B. et al., 2014. PASP, 126(938):398.

Hsu D.C. et al., 2019. AJ, 158(3):109.

Huang C.X. et al., 2018. *arXiv e-prints*, arXiv:1807.11129.

Jenkins J.M. et al., 2016. In G. Chiozzi and J.C. Guzman, editors, *Software and Cyberinfrastructure for Astronomy IV*, volume 9913 of *Society of Photo-Optical Instrumentation Engineers (SPIE) Conference Series*, 99133E.

Kipping D.M. et al., 2016. ApJ, 820(2):112.

Knutson H.A. et al., 2009. ApJ, 690(1):822–836.

Lendl M. et al., 2020. A&A, 643:A94.

Lillo-Box J., Millholland S., and Laughlin G., 2021. A&A, 654:A9.

Loeb A. and Gaudi B.S., 2003. ApJ, 588(2):L117–L120.

Lomb N.R., 1976. Ap&SS, 39(2):447–462.

Lovis C. and Fischer D., 2010. In S. Seager, editor, *Exoplanets*, 27–53.

Marcy G.W. and Butler R.P., 1996. ApJ, 464:L147.

Mayor M. and Queloz D., 1995. *Nature*, 378(6555):355–359.

Mayor M. et al., 2003. *The Messenger*, 114:20–24.

Mazeh T., 2008. In M.J. Goupil and J.P. Zahn, editors, *EAS Publications Series*, volume 29 of *EAS Publications Series*, 1–65.

Mazeh T. and Faigler S., 2010. A&A, 521:L59.

Millholland S. and Laughlin G., 2017. AJ, 154(3):83.

Montalto M. et al., 2021. A&A, 653:A98.

Naef D. et al., 2004. A&A, 414:351–359.

Nascimbeni V. et al., 2022. A&A, 658:A31.

Oberst T.E. et al., 2017. AJ, 153(3):97.

Patruno A. and Kama M., 2017. A&A, 608:A147.

Pepper J. et al., 2007. PASP, 119(858):923–935.

Pollacco D.L. et al., 2006. PASP, 118(848):1407–1418.

Queloz D. et al., 2001. *The Messenger*, 105:1–7.

Rauer H. et al., 2014. *Experimental Astronomy*, 38(1-2):249–330.

Ricker G.R. et al., 2014. In J. Oschmann Jacobus M., M. Clampin, G.G. Fazio, and H.A. MacEwen, editors, *Space Telescopes and Instrumentation 2014: Optical, Infrared, and Millimeter Wave*, volume 9143 of *Society of Photo-Optical Instrumentation Engineers (SPIE) Conference Series*, 914320.

Ricker G.R. et al., 2015. *Journal of Astronomical Telescopes, Instruments, and Systems*, 1:014003.

Rosenthal L.J. et al., 2021. ApJS, 255(1):8.

Sachs A., 1974. *Philosophical Transactions of the Royal Society of London. Series A, Mathematical and Physical Sciences*, 276(1257):43–50. ISSN 00804614.

Sackett P.D., 1999. In J.M. Mariotti and D. Alloin, editors, *Planets Outside the Solar System: Theory and Observations*, volume 532 of *NATO Advanced Study Institute (ASI) Series C*, 189.

Scargle J.D., 1982. ApJ, 263:835–853.

Sestovic M., Demory B.O., and Queloz D., 2018. A&A, 616:A76.

Shporer A., 2017. PASP, 129(977):072001.

Shporer A. et al., 2019. AJ, 157(5):178.

Siverd R.J. et al., 2012. ApJ, 761(2):123.

Smith J.C. et al., 2012. PASP, 124(919):1000.

Spiegel D.S., Burrows A., and Milsom J.A., 2011. ApJ, 727(1):57.

Stassun K.G. et al., 2019. AJ, 158(4):138.

Stumpe M.C. et al., 2012. PASP, 124(919):985.

Stumpe M.C. et al., 2014. PASP, 126(935):100.

Temple L.Y. et al., 2017. MNRAS, 471(3):2743–2752.

Udalski A. et al., 1992. Acta Astron., 42:253–284.

Venot O. et al., 2020. ApJ, 890(2):176.

Verschueren W., David M., and Griffin R.E.M., 1999. A&AS, 140:107–123.

Welsh W.F. et al., 2010. ApJ, 713(2):L145–L149.

Wheatley P.J. et al., 2018. MNRAS, 475(4):4476–4493.

Winn J.N., 2010. *arXiv e-prints*, arXiv:1001.2010.

Wolszczan A., 1994. *Science*, 264(5158):538–542.

Wolszczan A., 2008. *Physica Scripta Volume T*, 130:014005.

Wolszczan A. and Frail D.A., 1992. *Nature*, 355(6356):145–147.

Wong I. et al., 2020. AJ, 160(4):155.

Wong I. et al., 2021a. AJ, 162(6):256.

Wong I. et al., 2021b. AJ, 162(4):127.